






Chemical trends of deep levels in van der Waals semiconductors

Penghong Ci ^{1,2}, Xuezheng Tian ³, Jun Kang⁴, Anthony Salazar¹, Kazutaka Eriguchi¹, Sarah Warkander ¹, Kechao Tang¹, Jiaman Liu¹, Yabin Chen^{1,5}, Sefaattin Tongay⁶, Wladek Walukiewicz², Jianwei Miao ³, Oscar Dubon^{1,2} & Junqiao Wu ^{1,2}✉

Properties of semiconductors are largely defined by crystal imperfections including native defects. Van der Waals (vdW) semiconductors, a newly emerged class of materials, are no exception: defects exist even in the purest materials and strongly affect their electrical, optical, magnetic, catalytic and sensing properties. However, unlike conventional semiconductors where energy levels of defects are well documented, they are experimentally unknown in even the best studied vdW semiconductors, impeding the understanding and utilization of these materials. Here, we directly evaluate deep levels and their chemical trends in the bandgap of MoS₂, WS₂ and their alloys by transient spectroscopic study. One of the deep levels is found to follow the conduction band minimum of each host, attributed to the native sulfur vacancy. A switchable, DX center - like deep level has also been identified, whose energy lines up instead on a fixed level across different hosts, explaining a persistent photoconductivity above 400 K.

¹Department of Materials Science and Engineering, University of California, Berkeley, CA 94720, USA. ²Materials Sciences Division, Lawrence Berkeley National Laboratory, Berkeley, CA 94720, USA. ³Department of Physics & Astronomy and California NanoSystems Institute, University of California, Los Angeles, CA, USA. ⁴Beijing Computational Science Research Center, Beijing, China. ⁵School of Aerospace Engineering, Beijing Institute of Technology, Beijing, China. ⁶School for Engineering of Matter, Transport, and Energy, Arizona State University, Tempe, AZ 85287, USA. ✉email: wuj@berkeley.edu

Defects with energies falling within the bandgap may act as a trap or emitter of free charge carriers¹, a site for exciton recombination², and a center to scatter electrons or phonons³. In conventional semiconductors, native defects such as vacancies introduce levels close to the middle of the bandgap when the material is more covalently bonded, or close to the band edges when the material is more ionically bonded, resulting in the former materials being defect sensitive while the latter materials are relatively defect tolerant⁴. Comparing positions of defect levels across different host materials helps to reveal chemical trends that inform defect models with broad impact. For example, the deep level associated with a given impurity⁵ or native defect⁶ tends to lie universally at a fixed energy position with respect to the vacuum level even when doped in different semiconductors, which can be used to determine band alignments of the host materials; equilibrium native defects tend to drive the Fermi level toward a stabilization position, and this position with respect to the bandgap can be used as a descriptor of doping propensity and doping limit of the semiconductor⁷; the DX center, an metastable defect switchable between deep and shallow states, dominates the free electron density in III-V semiconductor alloys⁸. It is critical to ask whether such insights and knowledge attained in studying conventional semiconductors are applicable in vdW materials. New effects of defects may emerge because the layered nature of vdW materials allows stronger lattice relaxation as well as new types of defects such as intercalated atoms.

Scanning tunneling microscopy (STM) is able to experimentally visualize various types of defects on the surface and relate these imperfections to electronic structures in vdW crystals⁹, in particular for the most abundant native point defects that play a critical role in their electrical^{10–13}, optical², magnetic¹⁴, catalytic¹⁵ and sensing properties¹⁶. However, STM studies have led to inconsistency on the defect types with transmission electron microscopy investigations, as well as discrepancy in signatures of defect-induced mid-gap states from theoretical calculations^{1,3,17–21}, largely because of unclear differentiation of STM contrast between the metal and chalcogen sublattices and the complicated convolution of electronic and geometric structures⁹. Furthermore, it shows very limited capability in detecting defects beneath the surface.

In this work, we use deep level transient spectroscopy (DLTS), a high-frequency capacitance transient thermal scanning method^{22,23}, to characterize electronic structures of the deep traps inside the bandgap of vdW semiconductors, particularly MoS₂, WS₂ and their alloys, including their energy positions and capture cross sections. Combined with atomic-resolution scanning transmission electron microscopy and first-principles calculations, one of the deep levels determined by DLTS is identified as sulfur vacancies, whose energy position follows the conduction band edge in the host materials, distinct from vacancy defects in traditional group III-V semiconductors. A metastable DX center is identified in these vdW semiconductors, featuring a persistent photoconductivity above 400 K and explaining the chemical trend of native electron concentration in the hosts.

Results

DLTS devices and DLTS spectra. Mechanically exfoliated, multilayer (~ 50 nm) flakes of freshly grown Mo_{1-x}W_xS₂ ($x = 0, 0.4, 0.7, 1$) crystals were made into two-terminal Schottky-Ohmic devices (Fig. 1a). The Schottky contact was formed by dry-stamping freshly exfoliated flakes onto pre-deposited Pt electrodes and confirmed by the I - V and C - V curves shown in Fig. 1e, f, both of which show the n-type conductivity of MoS₂. This maximally protects the depletion region at the Schottky contact against contamination and damage²⁴, as it is at this region where

the deep levels trap and emit charge carriers during the DLTS measurement. The measured total capacitance (Supplementary Fig. 10) is composed of that of the DLTS device (C_{device}) and the stray capacitance (C_{stray}) connected in parallel. The latter, although with a large value, is insensitive to the external differential voltage (Supplementary Fig. 10), hence the variation of capacitance under the biased voltage indeed probes the former (Fig. 1f).

The depletion width at the Schottky junction (~ 20 nm, the shadow in Fig. 1d), hence the capacitance (Fig. 1c), is initially held constant by a steady-state reverse bias ($V_R = -0.5$ V, stage ①)²³. An opposite voltage pulse (V_P) is then added onto V_R , reducing the depletion width (as evidenced by the increased capacitance at less-negative voltage, Fig. 1f), and allowing the traps in the initial depletion region to be filled with free electrons (stage ②)²³. When the initial, constant bias is restored, the return of the capacitance to the steady-state value is characterized by a transient (stage ③) related to the emission of majority carriers from the deep traps in the material. The capacitance difference within a rate window (between the pre-set t_2 and t_1 in Fig. 1c)²² reaches the maximum at a specific temperature. The emission rate (e_n) in stage ③ depends exponentially on temperature via the trapping energy level (E_i) measured from the conduction band minimum (CBM, E_{CB})²²,

$$\frac{e_n}{T^2} = K\sigma_n \exp\left(-\frac{|E_{CB} - E_i|}{k_B T}\right) \quad (1)$$

where σ_n is the capture cross section, and K is a known constant. Arrhenius plots of Eq. (1) at various rate windows (0.5 ms to 20 ms in Fig. 2a) allow extraction of the activation energy of deep levels, $E_{CB} - E_i$. For MoS₂ we found two, 0.27 ± 0.03 eV (peak A) and 0.40 ± 0.02 eV (peak B), as shown in Fig. 2b. The positively valued DLTS peaks (Fig. 2a) indicates that these are majority carriers traps in MoS₂²². We also measured current transient spectroscopy (CTS, see Supplementary Fig. 1) by recording the current rather than capacitance under the pulsed bias²⁵, yielding an activation energy of $E_{CB} - E_i = 0.25 \pm 0.02$ eV for MoS₂ (Supplementary Fig. 1a), consistent with the peak A in DLTS. We note that for each of the trap energies obtained in this work, at least two devices were measured and all show consistently very similar energy. Thermodynamically, the slope of Eq. (1) corresponds to the change of enthalpy (ΔH), different from the Gibbs free energy $\Delta G (= E_{CB} - E_i)$ ²⁶, but the difference can be neglected when electrons are excited from the traps to the conduction band without invoking changes in the bonding configuration (see Supplementary Note 5)²⁷.

Determination of sulfur vacancies from STEM and DFT calculations. To reveal the atomic origin of these deep traps, we have performed first-principles calculations of S single vacancies (V_S) in multilayer MoS₂, WS₂ and their alloys. V_S is chosen because it is the most abundant defect known to naturally occur in these materials²¹. The calculation shows that V_S would introduce a deep-level state with energy of 0.29 eV (for MoS₂) and 0.21 eV (for WS₂) below the CBM, in good agreement with the DLTS/CTS results. We note that the value of 0.29 eV is also consistent with the calculated V_S energy in MoS₂ previously reported in literature^{1,3}. Our calculations also confirm that V_S is a deep acceptor, labeled as $(0/-)$ ^{1,23}, not responsible for the natively n-type conductivity of MoS₂. The neutral ground state implies its extremely weak Coulomb attraction to electrons, and hence very small capture cross section. V_S defects are directly observed in these materials by scanning transmission electron microscopy (STEM, Fig. 1b and Supplementary Fig. 5)¹¹, where the density of V_S is directly determined to be $1\sim 3 \times 10^{20} \text{ cm}^{-3}$

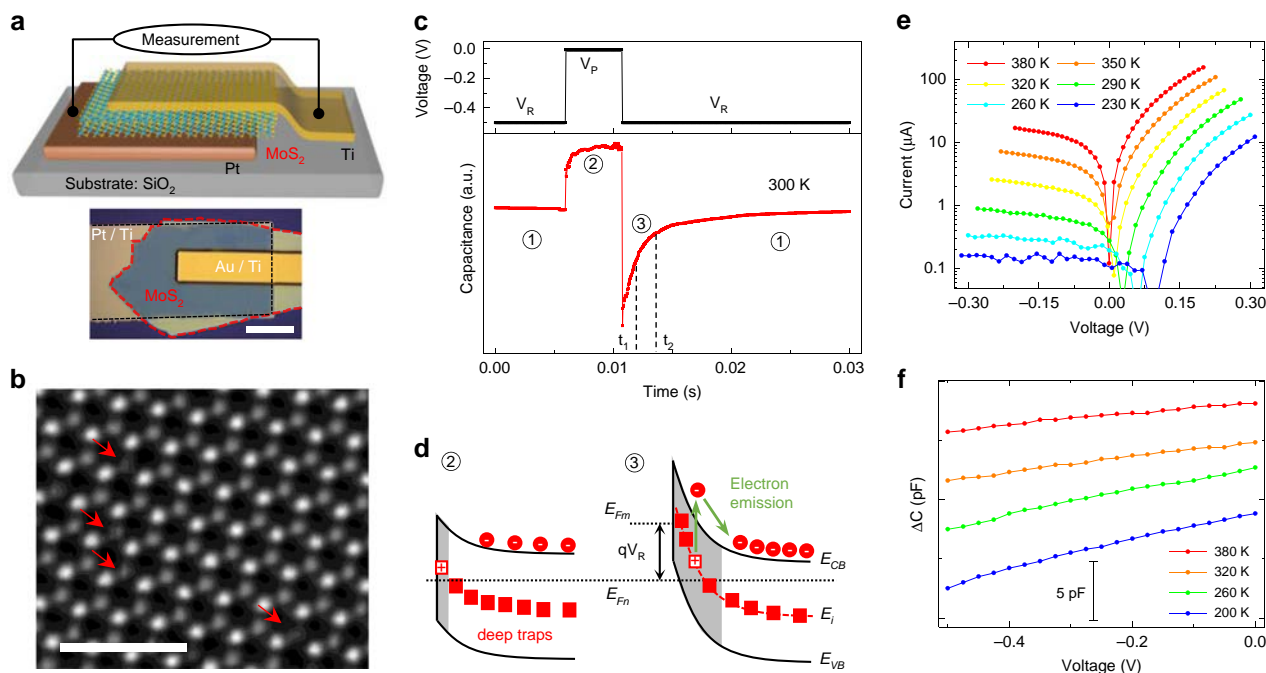


Fig. 1 Materials and devices for transient spectroscopic study of defects. **a** Schematic and optical image (scale bar: 20 μm) of an asymmetric MoS₂ device for DLTS, with Schottky contact (MoS₂/Pt/Ti) on the bottom and Ohmic contact (Au/Ti/MoS₂) on the top. **b** Aberration-corrected STEM image of a monolayer MoS₂ exfoliated from the materials used for devices. Red arrows highlight S vacancies (V_S). Scale bar, 1 nm. **c** Capacitance transient (bottom) in response to a pulsed change in bias voltage (top). **d** Band bending of the Schottky junction (MoS₂/Pt), illustrating the electron trapping (Ⓜ) and emission process (Ⓢ) of deep traps in the depletion region (shaded). V_R tunes the Fermi level of the n-type MoS₂ (E_{Fn}) with respect to that of the metal contact (E_{Fm}). **e** & **f**, Temperature-dependent I - V and C - V curves confirming the Schottky-Ohmic contacts.

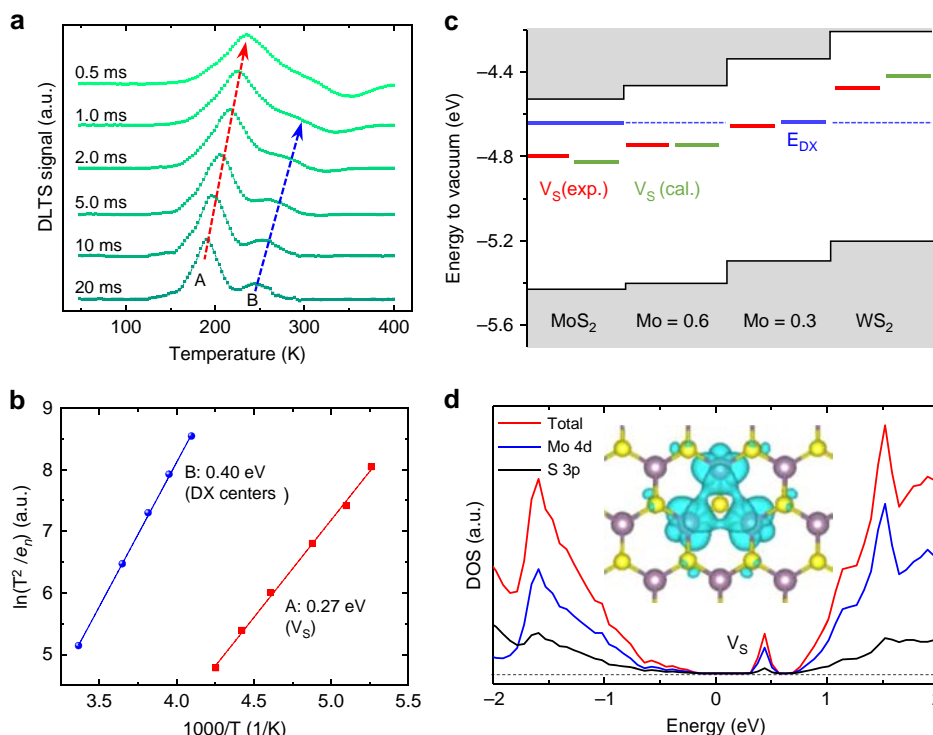


Fig. 2 Deep levels and their alignment in vdW crystals. **a** DLTS signal of a MoS₂ device at different rate windows and **b** the resultant Arrhenius plots to determine the activation energies. **c** Conduction and valence band edge alignment calculated with respect to the vacuum level, and positions of deep level experimentally identified in this work. Solid black lines: CBM and VBM in bulk crystals from our DFT calculations; red bars: deep levels attributed to V_S measured by DLTS and CTS; blue bars: DX center levels determined by DLTS and PPC (dashed blue line is guide to the eye); green bars: DFT-calculated V_S levels. **d** density of states (DOS) for multilayer MoS₂ with V_S . Inset: real space distribution of the wavefunction of V_S state. The purple and yellow spheres represent Mo and S atoms, respectively.

(Supplementary Fig. 4), on the same order of those reported in literature^{3,21}. The STEM study also confirms that V_S is the dominant point defects, and no other defects or impurities were detected in the materials. We note that akin to conventional semiconductors, not all of these V_S are electronically active (Supplementary Fig. 6); in fact, deep traps can be highly passivated or compensated, as observed in GaN and GaAs^{28,29}.

To reveal the chemical trend of the V_S level in different vdW semiconductors, $\text{Mo}_{0.6}\text{W}_{0.4}\text{S}_2$, $\text{Mo}_{0.3}\text{W}_{0.7}\text{S}_2$, and WS_2 were also synthesized and then assembled into Schottky devices for similar DLTS/CTS measurements (Supplementary Fig. 1). All of these materials exhibit at least one deep level, akin to the feature A observed in MoS_2 , with an energy level below the CBM of the host material of 0.29 ± 0.02 eV, 0.31 ± 0.02 eV and 0.26 ± 0.04 eV (red bars in Fig. 2c), respectively. These energy levels are all in good agreement with the DFT calculated V_S levels, as shown by the green bars in Fig. 2c and the refined band structure with V_S in Supplementary Fig. 8.

Some deep levels in different isovalent materials line up at a fixed position with respect to the vacuum level, such as oxygen dopant or Ga dangling bond in different $\text{GaAs}_{1-x}\text{P}_x$ alloys^{6,30}. In contrast, the red bars in Fig. 2c show that as the W fraction increases in $\text{Mo}_{1-x}\text{W}_x\text{S}_2$, the energy level of V_S shifts monotonically toward the vacuum level; that is, the V_S level largely follows the CBM of the host. This is understandable because, as shown in the partial density of states plot in Fig. 2d, the V_S state originates mostly from the 4d (5d) orbitals of the Mo (W) atoms, rather than the S atoms, sharing the same orbital composition as the CBM^{31,32}. Following this finding, anion impurities (such as oxygen) substituting S are predicted to create deep levels also about 0.3 eV below the CBM of the host (see Supplementary Fig. 7), because it is known that highly electronegative, substitutional dopants tend to have similar wavefunctions as those of ideal vacancies⁶. The electron capture cross section (σ_n) of V_S is evaluated from Eq. (1) to be $\sim 3.6 \times 10^{-18}$ cm² in MoS_2 , using the thermal velocity effective mass ($0.57 m_0$) and effective density of states mass ($0.50 m_0$) obtained from our DFT calculation and literature (see Supplementary Note 1). This value is small but comparable to that of Zn acceptor level in Si and Cu acceptor level in Ge^{23,33}.

Persistent photoconductivity and DX center model. To explore the origin of peak B (0.40 eV) in MoS_2 shown in Fig. 2a, we obtained complementary information about deep levels from photoconductivity measurements. Photoconductivity, especially when it is persistent (persistent photoconductivity, PPC), has been used to gauge conduction by charge carriers photo-liberated from certain deep traps^{34,35}. Figure 3a shows temperature-dependent dark conductance of a MoS_2 flake (~ 50 nm thick) measured in four-probe geometry (Inset of Fig. 3b). The sample was cooled in darkness from 400 K to 200 K (black data points). It was then exposed to white light for 10 min (blue data point) at 200 K, during which the conductance became two orders of magnitude higher than in the dark. When the light was switched off (dark again) at this low temperature, the conductance dropped slightly, but still stayed >50 times higher than the pristine dark state. The PPC stayed at this level for at least 11 h at 200 K (Fig. 3b). When the sample was warmed up, the conductance stayed at the higher level (red data points) until a temperature of 400 K where it nearly converged to the pristine dark conductance.

Such a PPC effect in response to light exposure and temperature is a direct manifestation of metastability of defect states, and a hallmark of DX centers in semiconductors^{34,35}. DX centers, observed in the 1980s in many III-V semiconductors such as AlGaAs, are a special type of localized states resonant

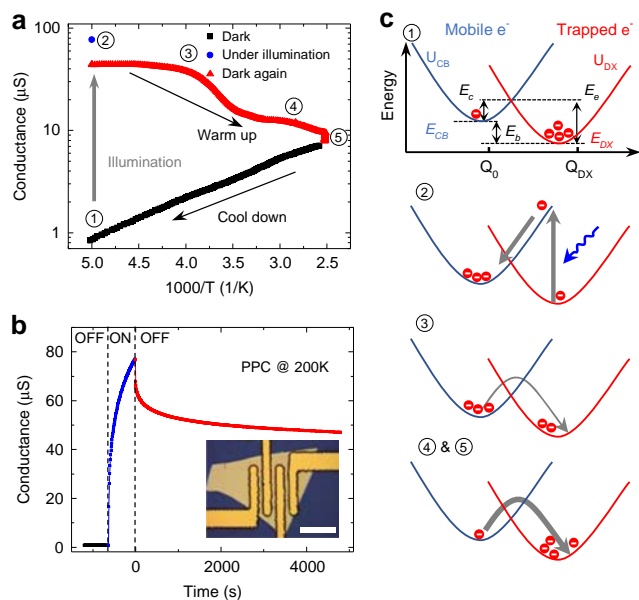


Fig. 3 Temperature-dependent persistent photoconductivity (PPC) and the DX center model. **a** Conductance of a MoS_2 device as a function of temperature before, during, and after exposure to light illumination. **b** PPC temperature of the device at 200 K. Inset: optical image of a four-probe device for PPC measurement (scale bar: 20 μm). **c** Configurational coordinate diagram (CCD) showing the three energies to characterize the DX center and describe the five PPC processes in **a**.

with the conduction band of the host⁸. In contrast to ordinary deep levels, DX centers are capable of switching into a charge-delocalized, electron-donating state via significant lattice relaxation when triggered by external stimuli, such as light and gate control^{8,36,37}. Typically described in the configurational coordinate diagram (CCD) as shown in Fig. 3c, DX centers are characterized by a parabolic coordinate (Q) dependence of DX center energy (U_{DX}) intersecting that of the delocalized state (U_{CB})⁸. The displacement along the Q axis between the two minima describes a large lattice relaxation that reflects the metastability of the DX centers. Three energies are thus defined: capture activation energy (E_c), which is the energy barrier for the DX center to trap an electron and can be determined from the kinetics of PPC; emission activation energy (E_e), the energy barrier to de-trap (emit) an electron, measured via DLTS^{8,36}; and energy depth ($E_b = E_{CB} - E_{DX} = E_e - E_c$), which is the ground state energy (E_{DX}) measured from the CBM (E_{CB}) and can be derived from the temperature dependence of conductance.

As shown in Fig. 3a, c, at the thermal equilibrium state (stage ①), most electrons are trapped in the DX centers. Upon excitation by light with energies above the optical threshold (stage ②)^{8,36}, electrons in E_{DX} are photo-excited to E_{CB} . When the light is off, these electrons stay in E_{CB} and are blocked by the barrier E_c from relaxing back to E_{DX} , causing the PPC (stage ③). When temperature rises, more electrons are thermally excited over E_c into E_{DX} (stage ④), eventually recovering to the pristine, dark-state conductivity (stage ⑤). In this study, the PPC effect exists at temperatures up to more than 400 K (upper limit of our equipment). This is in stark contrast to the PPC effect of DX centers discovered in group III-V semiconductors, where it survives only at $T < \sim 140$ K^{35,37,38}.

The transient PPC curves are plotted in Fig. 4a for a range of temperatures, where non-persistent photocurrent was excluded, dark current was subtracted and the remaining part was normalized by the value at $t = 0$, the moment the illumination

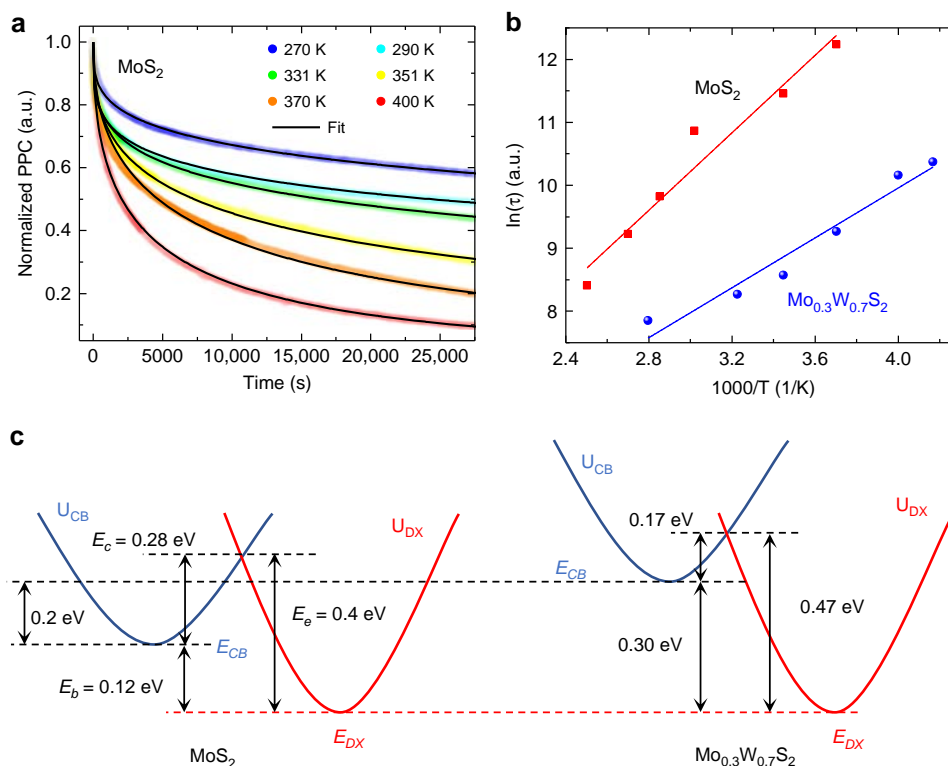


Fig. 4 DX center levels measured in MoS₂ and Mo_{0.3}W_{0.7}S₂. **a** Transient normalized-PPC curves at various temperatures for MoS₂ and **b** the resultant Arrhenius plots of the time constant for MoS₂ and Mo_{0.3}W_{0.7}S₂. Semitransparent points: experimental data; thin solid lines: fitting to Eq. (2). **c** CCD for MoS₂ and Mo_{0.3}W_{0.7}S₂, where the energy depth (E_b), capture (E_c) and emission (E_e) energy barriers are determined by temperature dependence of conductance, PPC and DLTS, respectively. The band offset between the two materials is obtained from DFT, resulting in a flat lineup of the DX center energy level (E_{DX}) across different host materials. The error range for these energies is estimated to be ± 0.04 eV.

is terminated. Note that in order to reset the initial dark current before taking each of these PPC curves, the samples were kept at 400 K for at least one day in a high vacuum ($\sim 10^{-6}$ torr) to drain the extra electrons in E_{CB} . We see that, consistent with the DX center model (Fig. 3), high temperature expedites the kinetics of the PPC decay. Following the treatment in literature, the PPC can be well described by the stretched-exponential equation^{34,35}:

$$I_{PPC}(t)/I_{PPC}(0) = \exp[-(t/\tau)^\beta] \quad (2)$$

where τ is the characteristic decay time constant, β is a decay index with a value between 0 and 1. Because of the underlying thermal activation process, the temperature dependence of τ is related to the trap barrier via $\tau \propto \exp(E_c/k_B T)$ ^{34,35}. Arrhenius plots of the temperature-dependent τ yield E_c of 0.28 ± 0.02 eV for MoS₂ and 0.17 ± 0.02 eV for Mo_{0.3}W_{0.7}S₂ (Fig. 4b and Supplementary Fig. 3). These values are higher than E_c (~ 0.14 eV) of DX centers reported in the Se-doped AlGaAs system⁸, presumably because the layered structure of the vdW materials allows larger lattice relaxation than the tetrahedral structure of AlGaAs. The higher E_c is also responsible for the extension of PPC to much higher temperatures.

The energy E_b ($= E_{CB} - E_{DX}$) characterizes the thermodynamic energy depth of the DX center, and was extracted from Arrhenius plots of the dark conductance of the sample (Supplementary Fig. 3). Values of $E_b = 0.12$ eV and 0.30 eV were found for MoS₂ and Mo_{0.3}W_{0.7}S₂, respectively. Adding E_b to E_c gives E_e , the emission barrier, of 0.39 eV and 0.47 eV for MoS₂ and Mo_{0.3}W_{0.7}S₂, respectively. These values are in very good agreement with the energies of peak B measured in DLTS for MoS₂ (0.40 ± 0.02 eV) and Mo_{0.3}W_{0.7}S₂ (0.47 ± 0.02 eV). Therefore, we attribute the peak B measured in DLTS to emission of

electrons from the DX centers. We note that, unlike regular deep levels (such as the V_S state) which have no capture/emission barriers, for DX centers, the Arrhenius plot of the DLTS spectrum extracts the emission barrier E_e (Figs. 2c and 3c), rather than E_b , which is the separation of E_{DX} directly measured from the conduction or valence band edges (see more in Supplementary Note 6)²³. Following the CBM offset of ~ 0.3 eV between MoS₂ and WS₂ from our DFT calculation, the CBM (E_{CB}) of Mo_{0.3}W_{0.7}S₂ is interpolated to be higher than that of MoS₂ by 0.2 eV. Combining all these energy values, the energy of E_{DX} shows an interestingly flat alignment across these two compositions, as plotted in the CCD in Fig. 4c. It is not surprising to see that the E_{DX} position is independent of the material composition because it is also constant for DX centers in AlGaAs across different alloy compositions^{8,36,38}: in AlGaAs alloys, E_{DX} is located universally at 3.8 eV below the vacuum level, and does not follow the CBM of the host material (in contrast to shallow defect levels). DX centers act as deep traps that result in different shallow donor doping efficiency in AlGaAs with different compositions⁸; similarly, the chemical trend of energy level of DX centers in the vdW semiconductors can explain the well-known, orders of magnitude higher native free electron density in undoped MoS₂ than in WS₂, as the DX centers are shallower in the former (details in Supplementary Fig. 9). When they are doped, these deep defects also largely determine the doping efficiency and dopability of these materials, as they can compensate the shallow dopants.

Discussion

Although our multipronged experiments show clear evidence of DX centers in these vdW semiconductors, elucidation of the

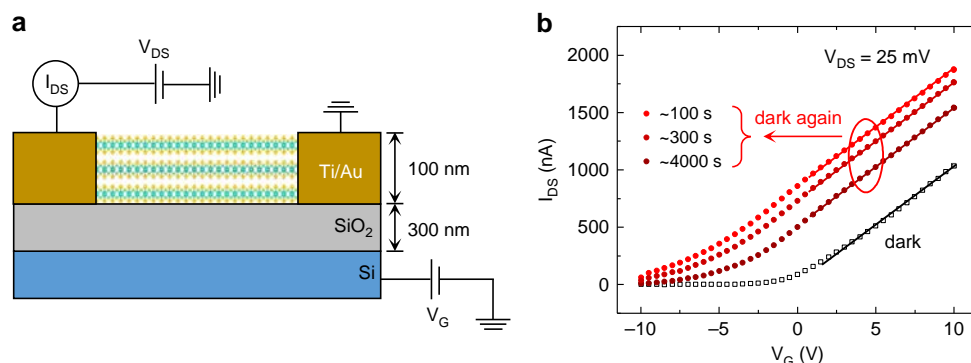


Fig. 5 Mobility of MoS₂ before and after illumination. **a** Schematic of a multilayer MoS₂ field-effect transistor (FET). **b** Transient transfer characteristics for the FET before the illumination (hollow points) and at specific time after the illumination is turned off (solid points). The back gate voltage, V_G , is applied to the substrate. The solid lines show the slopes of the I_{DS} - V_G curves, corresponding to electron mobility of the channel material in the device.

atomic origin of the DX centers requires further exploration including extensive first-principles calculations. However, the flat alignment of E_{DX} provides a clue. In AlGaAs, the electron wavefunction of the DX center is extremely localized on an Al/Ga site surrounded only by and bonded only to the nearest As atoms; therefore, E_{DX} is very insensitive to the change of Al fraction in the alloy^{37,39}. Similarly, in Mo_{1-x}W_xS₂ alloys where E_{DX} is independent of the cation composition x , it is likely that the DX centers neighbor only S atoms, hence are either impurity atoms substituting the cation, or small interstitial atoms bonded to S. For example, a potential candidate would be a defect complex involving hydrogen bonded to S, a dopant inevitably and unintentionally introduced during the growth. Indeed, hydrogen has been proposed to be a possible origin of n-type native conductivity in MoS₂ due to the formation of shallow levels⁴⁰.

The decay time constant describes the time it takes for the mobile electrons to be re-trapped by the DX centers, and dictates the relaxation kinetics of the free charge carrier density. The transient conductivity or current in the PPC (Fig. 4a) is assumed to have a similar relaxation kinetics as that of free carrier density, and hence can be used to extract the delay time constant for DX centers. This assumption is typically made in investigation of DX centers in traditional III-V semiconductors as the carrier mobility varies much less than the carrier density and the current is then directly proportional to carrier density^{34–36,41,42}. In order to test the validity of this assumption in our case, a multilayer MoS₂ FET was made to determine the evolution of mobility before and after the illumination. Figure 5a depicts a multilayer MoS₂ assembled into the FET which is subjected to a back gate voltage (V_G). According to the data in Fig. 5b, we extract the low-field field-effect mobility to be ~ 16 cm²/(V S) for the MoS₂ channel, based on the expression $\mu = [dI_{DS}/dV_{Gate}] \times [L/WCV_{DS}]$ ⁴³, where W and L are the width and length of the channel, respectively, C is the capacitance of the gate dielectric SiO₂ layer, and V_{DS} is the source-drain voltage in the FET. These I_{DS} - V_G curves exhibit the same slope before and after light illumination, indicating a constant mobility regardless of the density of free or trapped electrons in the channel, hence validating the extraction of time constant from electrical current via Eq. (2).

It is technically challenging to apply the DLTS to monolayers of vdW semiconductors, owing to expected high leakage current and issues arising from the sub-depletion width thickness. However, the deep levels we quantified for thick layers are expected to be applicable to monolayers and few layers. This is because the very weak interlayer vdW coupling only modulates the conduction and valence band edges, transitioning the material from direct bandgap in monolayers to indirect bandgap in the

bulk, while hardly affecting the entire band structure³²; on the other hand, the spatially very localized wavefunctions of deep levels do not hybridize with the conduction or valence band edges, which is in contrast to shallow defects whose wavefunctions are composed of entirely the band edge states. For example, regarding monolayer MoS₂, first-principles calculations predicted that the V_S deep level lies about 0.5 eV below the CBM at the K point in the Brillouin Zone^{1,3,17,21,44}, which is in good agreement with the 0.27 eV below the CBM at the Q point in multilayer MoS₂ quantified in this study, considering the 0.2 eV CBM offset between monolayer and bulk MoS₂^{45,46}.

Our work determines energy levels and chemical trends of the most abundant native defects in MoS₂, WS₂ and their alloys. These energy levels offer quantitative references for both applications that are limited by defects such as transistors^{10,24} and light emitting devices², as well as applications that are facilitated by defects such as catalysis¹⁵ and sensors¹⁶. We also discover metastable and switchable, DX center-like defects in these vdW materials at temperatures above 400 K, in contrast to those in other semiconductors that exist only at $T < 140$ K^{8,38}. As a result, practical device applications may be developed from the DX centers in vdW materials, such as nonvolatile memory based on a single defect. These defects may provide a platform for study of electron-phonon coupling, electron correlation, and many-body physics such as negative-U effects in quasi-two-dimensional crystals³⁰.

Methods

Materials preparation. The vdW bulk crystals were synthesized using the flux zone technique without using transporting agent precursor, in order to reduce contamination⁴⁷. The growth starts with 6N-purity, commercially available 300 mesh amorphous powders of molybdenum and/or tungsten and pieces of sulfur. Further electrolytic purification was necessary to eliminate magnetic impurities commonly found in metal powders, and secondary ion mass spectroscopy (SIMS) was used to test the purity. Powders were mixed at stoichiometric ratios, sealed under 10^{-7} torr pressure in quartz ampoules, and annealed up to 800 °C for 10 days. The polycrystalline products were collected and resealed again. In the second formation process, a small temperature differential (~ 15 °C) was created at high temperatures to thermodynamically drive the reactions. The crystallization process was slow and the entire growth was completed in a three-month time frame.

Device fabrication. Multilayer (~ 50 nm thick) MoS₂, WS₂ and their alloys were mechanically exfoliated from bulk crystals. For DLTS/CTS experiments, these samples were transferred onto Pt/Ti (45/10 nm) bottom electrodes¹⁰, followed by photolithography, and electron beam evaporation of 20-nm Ti and then 80-nm Au as the top electrodes, and lift-off. In this way, the vdW flake is sandwiched by Pt (Schottky) metal at the bottom, and Ti (Ohmic) metal at the top. For PPC measurements, four-probe metal leads (Au (80 nm)/Ti (20 nm), Ti at bottom) were deposited onto exfoliated samples. The devices used SiO₂ (300 nm)/Si as the substrate.

Electrical measurements. A deep level transient spectrometer (Sula Technologies) was used to measure DLTS, CTS, CV, and IV curves in Figs. 1 and 2. In this instrument, the emission rate is set as $e_n = 1/(D \times \Delta t)$, where $\Delta t = t_2 - t_1$ is the preset time difference in Figs. 1c and 2a, and D is a constant representing the delay factor, 1.94 and 4.3 for the DLTS and CTS measurements, respectively. In the capacitance test, including CV and DLTS, an A.C. voltage with an amplitude of ~60 mV and frequency of 1 MHz was superimposed onto the D.C. reverse bias. For the PPC measurements, four-terminal transport characteristics were measured by applying a DC bias to the outer channel and recording the current using a current amplifier and the voltage drop across the inner channel using a voltage amplifier. Optical illumination for the PPC was by a convection-cooled 30-Watt illuminator (Fiber-Lite 190).

STEM characterization. Mechanically-exfoliated monolayer MoS₂ was transferred from SiO₂ surface to TEM grids (Quantifoil R2/2) by selective etching of the SiO₂ in 49% hydrofluoric acid. Images were acquired from different regions of the monolayer MoS₂ using a Nion UltraSTEM 100 aberration-corrected STEM in ADF-STEM mode with $E = 70$ kV. The beam convergence semi-angle was 30 mrad and the detector collection angle was in the range of 30–300 mrad, where a small detector inner angle was chosen to reduce the electron dose. The energy spread of the electron beam was 0.3 eV. To reduce the total electron dose, images were measured with a beam current of 15 pA and a dwell time of 84 μ s per image, which correspond to a total electron dose 4.7×10^5 e⁻/Å². The ADF-STEM images contain a mixture of Poisson and Gaussian noise and were denoised by the block-matching and 3D filtering (BM3D) algorithm⁴⁸, from which S vacancies were identified. It has been reported previously that a 80 keV electron beam induces S vacancies in MoS₂ with a rate of 3.45×10^8 – 3.36×10^9 electrons per S vacancy^{3,21}. As we used a 70 keV electron beam, the vacancy formation rate in our experiment should be $>3.45 \times 10^8$ electrons per S vacancy. From the total electron dose used in our experiment, we estimated the electron beam induced S vacancy density in our sample was $<2 \times 10^{20}$ cm⁻³. Since we observed a S vacancy density of 3×10^{20} cm⁻³ in the MoS₂ sample, we concluded that the native S vacancy density was $>1 \times 10^{20}$ cm⁻³, which is in agreement with that of exfoliated undoped MoS₂ samples²¹.

DFT calculations. The calculations were performed using the Vienna ab initio simulation package (VASP) with the projector-augmented wave method^{49,50}. The generalized gradient approximation of Perdew-Burke-Ernzerhof (GGA-PBE) was adopted for the exchange-correlation functionals⁵¹. The energy cutoff for the plane-wave expansion was set to 350 eV. Structure relaxation was stopped when the force on each atom was smaller than 0.01 eV/Å. The van der Waals interaction was included by using the correction scheme of Grimme⁵².

For defect calculations in bulk MX₂, we employed $5 \times 5 \times 1$ supercell, where a tilted c lattice vector was adopted, with $c = c_0 + 2a_0 + 2b_0$, where a_0 , b_0 , and c_0 are the primitive cell lattice vectors. As discussed in previous studies¹, this improves the convergence of total energies with respect to cell size. The k-point sampling is $2 \times 2 \times 2$. The defect charge-transition energy level $\epsilon(q/q')$ corresponds to the Fermi energy E_F at which the formation energy for a defect α with different charge state q and q' equals with each other. It can be calculated by⁵³:

$$\epsilon(q/q') = [E(\alpha, q) - E(\alpha, q') + (q - q')(E_{VB} + \Delta V)] / (q' - q).$$

Here $E(\alpha, q)$ is the total energy of the supercell containing the defect, and E_{VB} is the valence band maximum (VBM) energy of the host material. The potential alignment correction term ΔV is added to align the VBM energy in systems with different charged states. It is calculated by the energy shift of the 1s core-level energy of a specified atom (which is far away from the defect site) between the neutral defect and charged cases. For Mo_{1-x}W_xS₂ alloys, different S vacancy sites have different local environments. The number of surrounding Mo and W atoms varies, resulting in four types of V_S. We calculated the charge-transition levels for each type, and then carried out an average according to the concentration of different types to obtain the final charge-transition level.

Data availability

The data that support the plots in this paper are available from the corresponding author upon reasonable request.

Received: 28 May 2020; Accepted: 2 October 2020;

Published online: 23 October 2020

References

- Komsa, H.-P. & Krasheninnikov, A. V. Native defects in bulk and monolayer MoS₂ from first principles. *Phys. Rev. B* **91**, 125304 (2015).
- Amani, M. et al. Near-unity photoluminescence quantum yield in MoS₂. *Science* **350**, 1065–1068 (2015).
- Qiu, H. et al. Hopping transport through defect-induced localized states in molybdenum disulphide. *Nat. Commun.* **4**, 1–6 (2013).
- Pandey, M. et al. Defect-tolerant monolayer transition metal dichalcogenides. *Nano Lett.* **16**, 2234–2239 (2016).
- Langer, J. M. & Heinrich, H. Deep-level impurities: a possible guide to prediction of band-edge discontinuities in semiconductor heterojunctions. *Phys. Rev. Lett.* **55**, 1414 (1985).
- Hjalmarson, H. P., Vogl, P., Wolford, D. J. & Dow, J. D. Theory of substitutional deep traps in covalent semiconductors. *Phys. Rev. Lett.* **44**, 810 (1980).
- Walukiewicz, W. Amphoteric native defects in semiconductors. *Appl. Phys. Lett.* **54**, 2094–2096 (1989).
- Mooney, P. Deep donor levels (DX centers) in III-V semiconductors. *J. Appl. Phys.* **67**, R1–R26 (1990).
- Barja, S. et al. Identifying substitutional oxygen as a prolific point defect in monolayer transition metal dichalcogenides. *Nat. Commun.* **10**, 1–8 (2019).
- Cui, X. et al. Multi-terminal transport measurements of MoS₂ using a van der Waals heterostructure device platform. *Nat. Nanotechnol.* **10**, 534 (2015).
- Tian, X. et al. Correlating the three-dimensional atomic defects and electronic properties of two-dimensional transition metal dichalcogenides. *Nat. Mater.* **19**, 867–873 (2020).
- Amit, I. et al. Role of charge traps in the performance of atomically thin transistors. *Adv. Mater.* **29**, 1605598 (2017).
- Yin, L. et al. Robust trap effect in transition metal dichalcogenides for advanced multifunctional devices. *Nat. Commun.* **10**, 1–8 (2019).
- Ramasubramaniam, A. & Naveh, D. Mn-doped monolayer MoS₂: an atomically thin dilute magnetic semiconductor. *Phys. Rev. B* **87**, 195201 (2013).
- Le, D., Rawal, T. B. & Rahman, T. S. Single-layer MoS₂ with sulfur vacancies: structure and catalytic application. *J. Phys. Chem. C* **118**, 5346–5351 (2014).
- Xie, J. et al. Defect-rich MoS₂ ultrathin nanosheets with additional active edge sites for enhanced electrocatalytic hydrogen evolution. *Adv. Mater.* **25**, 5807–5813 (2013).
- Vancsó, P. et al. The intrinsic defect structure of exfoliated MoS₂ single layers revealed by scanning tunneling microscopy. *Sci. Rep.* **6**, 29726 (2016).
- Addou, R., Colombo, L. & Wallace, R. M. Surface defects on natural MoS₂. *ACS Appl. Mater. Interfaces* **7**, 11921–11929 (2015).
- Liu, X., Balla, I., Bergeron, H. & Hersam, M. C. Point defects and grain boundaries in rotationally commensurate MoS₂ on epitaxial graphene. *J. Phys. Chem. C* **120**, 20798–20805 (2016).
- Jeong, T. Y. et al. Spectroscopic studies of atomic defects and bandgap renormalization in semiconducting monolayer transition metal dichalcogenides. *Nat. Commun.* **10**, 1–10 (2019).
- Hong, J. et al. Exploring atomic defects in molybdenum disulphide monolayers. *Nat. Commun.* **6**, 1–8 (2015).
- Lang, D. Deep-level transient spectroscopy: a new method to characterize traps in semiconductors. *J. Appl. Phys.* **45**, 3023–3032 (1974).
- McCluskey, M. D. & Haller, E. E. *Dopants and defects in semiconductors*. (CRC press, 2018).
- Liu, Y. et al. Approaching the Schottky–Mott limit in van der Waals metal–semiconductor junctions. *Nature* **557**, 696–700 (2018).
- Borsuk, J. & Swanson, R. Current transient spectroscopy: a high-sensitivity DLTS system. *IEEE Trans. Electron Devices* **27**, 2217–2225 (1980).
- Blood, P. & Orton, J. W. *The electrical characterization of semiconductors: majority carriers and electron states*. 2 (Academic press, London, 1992).
- Almbladh, C.-O. & Rees, G. Statistical mechanics of electronic energy levels in semiconductors. *Solid State Commun.* **41**, 173–176 (1982).
- Lagowski, J., Kaminska, M., Parsey, J. Jr., Gatos, H. & Lichtensteiger, M. Passivation of the dominant deep level (EL2) in GaAs by hydrogen. *Appl. Phys. Lett.* **41**, 1078–1080 (1982).
- Vertiatchikh, A., Eastman, L., Schaff, W. & Prunty, T. Effect of surface passivation of AlGaIn/GaN heterostructure field-effect transistor. *Electron. Lett.* **38**, 388–389 (2002).
- Yu, P. Y. & Cardona, M. *Fundamentals of semiconductors: physics and materials properties*. (Springer, 1996).
- Kang, J., Tongay, S., Zhou, J., Li, J. & Wu, J. Band offsets and heterostructures of two-dimensional semiconductors. *Appl. Phys. Lett.* **102**, 012111 (2013).
- Ci, P. et al. Quantifying van der Waals interactions in layered transition metal dichalcogenides from pressure-enhanced valence band splitting. *Nano Lett.* **17**, 4982–4988 (2017).
- Claeys, C. & Simoen, E. *Germanium-based technologies: from materials to devices*. (Elsevier, 2011).
- Li, J. et al. Nature of Mg impurities in GaN. *Appl. Phys. Lett.* **69**, 1474–1476 (1996).
- Lin, J., Dissanayake, A., Brown, G. & Jiang, H. Relaxation of persistent photoconductivity in Al_{0.3}Ga_{0.7}As. *Phys. Rev. B* **42**, 5855 (1990).
- McCluskey, M. et al. Metastability of oxygen donors in AlGaIn. *Phys. Rev. Lett.* **80**, 4008 (1998).
- Chadi, D. & Chang, K.-J. Theory of the atomic and electronic structure of DX centers in GaAs and Al_xGa_{1-x}As alloys. *Phys. Rev. Lett.* **61**, 873 (1988).

38. Chand, N. et al. Comprehensive analysis of Si-doped Al_xGa_{1-x}As (x= 0 to 1): Theory and experiments. *Phys. Rev. B* **30**, 4481 (1984).
39. Chadi, D. & Chang, K.-J. Energetics of DX-center formation in GaAs and Al_xGa_{1-x}As alloys. *Phys. Rev. B* **39**, 10063 (1989).
40. Singh, A. & Singh, A. K. Origin of n-type conductivity of monolayer MoS₂. *Phys. Rev. B* **99**, 121201 (2019).
41. Fujisawa, T., Kristofik, J., Yoshino, J. & Kukimoto, H. Metastable behavior of the DX center in Si-doped GaAs. *Jpn. J. Appl. Phys.* **27**, L2373 (1988).
42. Tachikawa, M. et al. Observation of the persistent photoconductivity due to the DX center in GaAs under hydrostatic pressure. *Jpn. J. Appl. Phys.* **24**, L893 (1985).
43. Radisavljevic, B., Radenovic, A., Brivio, J., Giacometti, V. & Kis, A. Single-layer MoS₂ transistors. *Nat. Nanotechnol.* **6**, 147 (2011).
44. Chen, Y. et al. Tuning electronic structure of single layer MoS₂ through defect and interface engineering. *ACS Nano* **12**, 2569–2579 (2018).
45. Liu, G.-B., Xiao, D., Yao, Y., Xu, X. & Yao, W. Electronic structures and theoretical modelling of two-dimensional group-VIB transition metal dichalcogenides. *Chem. Soc. Rev.* **44**, 2643–2663 (2015).
46. Guo, Y. & Robertson, J. Band engineering in transition metal dichalcogenides: Stacked versus lateral heterostructures. *Appl. Phys. Lett.* **108**, 233104 (2016).
47. Wang, G. et al. Spin-orbit engineering in transition metal dichalcogenide alloy monolayers. *Nat. Commun.* **6**, 1–7 (2015).
48. Dabov, K., Foi, A., Katkovnik, V. & Egiazarian, K. Image denoising by sparse 3-D transform-domain collaborative filtering. *IEEE Trans. Image Process.* **16**, 2080–2095 (2007).
49. Kresse, G. & Furthmüller, J. Efficient iterative schemes for ab initio total-energy calculations using a plane-wave basis set. *Phys. Rev. B* **54**, 11169 (1996).
50. Blöchl, P. E. Projector augmented-wave method. *Phys. Rev. B* **50**, 17953 (1994).
51. Perdew, J. P., Burke, K. & Ernzerhof, M. Generalized gradient approximation made simple. *Phys. Rev. Lett.* **77**, 3865 (1996).
52. Grimme, S. Semiempirical GGA-type density functional constructed with a long-range dispersion correction. *J. Comput. Chem.* **27**, 1787–1799 (2006).
53. Wei, S.-H. Overcoming the doping bottleneck in semiconductors. *Comput. Mater. Sci.* **30**, 337–348 (2004).

Acknowledgements

This work was supported by the Electronic Materials Program funded by the Director, Office of Science, Office of Basic Energy Sciences, Materials Sciences and Engineering Division, of the U.S. Department of Energy under Contract No. DE-AC02-05CH11231. The device fabrication was partly supported by the Center for Energy Efficient Electronics Science (NSF Award No. 0939514). J.M. and X.T. acknowledge the support by the US Department of Energy, Office of Science, Basic Energy Sciences, Division of Materials Sciences and Engineering under award DE-SC0010378 and by an Army Research Office MURI grant on Ab-Initio Solid-State Quantum Materials: Design, Production and Characterization at the Atomic Scale (18057522). We are grateful for Prof. Mary Scott

and Dr. Yaqian Zhang for assistance in TEM, and Dr. Muhua Sun for drawing the schematic of the DLTS device.

Author contributions

P.C., O.D. and J.W. conceived this project. P.C. fabricated DLTS and PPC devices and completed the measurements, with the assistance from A.S., K.E., S.W., K.T., J.L., Y.C. and O.D. X.T. and J.M. contributed to atomic-resolution STEM imaging. S.T. grew the bulk MoS₂, WS₂ and alloys. J.K. performed DFT calculations. P.C., J.K., W.W. and J.W. analyzed the results. All authors discussed and contributed to the preparation of the manuscript.

Competing interests

The authors declare no competing interests.

Additional information

Supplementary information is available for this paper at <https://doi.org/10.1038/s41467-020-19247-1>.

Correspondence and requests for materials should be addressed to J.W.

Peer review information *Nature Communications* thanks Abdelmajid Mesli and the other, anonymous reviewer(s) for their contribution to the peer review of this work. Peer review reports are available.

Reprints and permission information is available at <http://www.nature.com/reprints>

Publisher's note Springer Nature remains neutral with regard to jurisdictional claims in published maps and institutional affiliations.

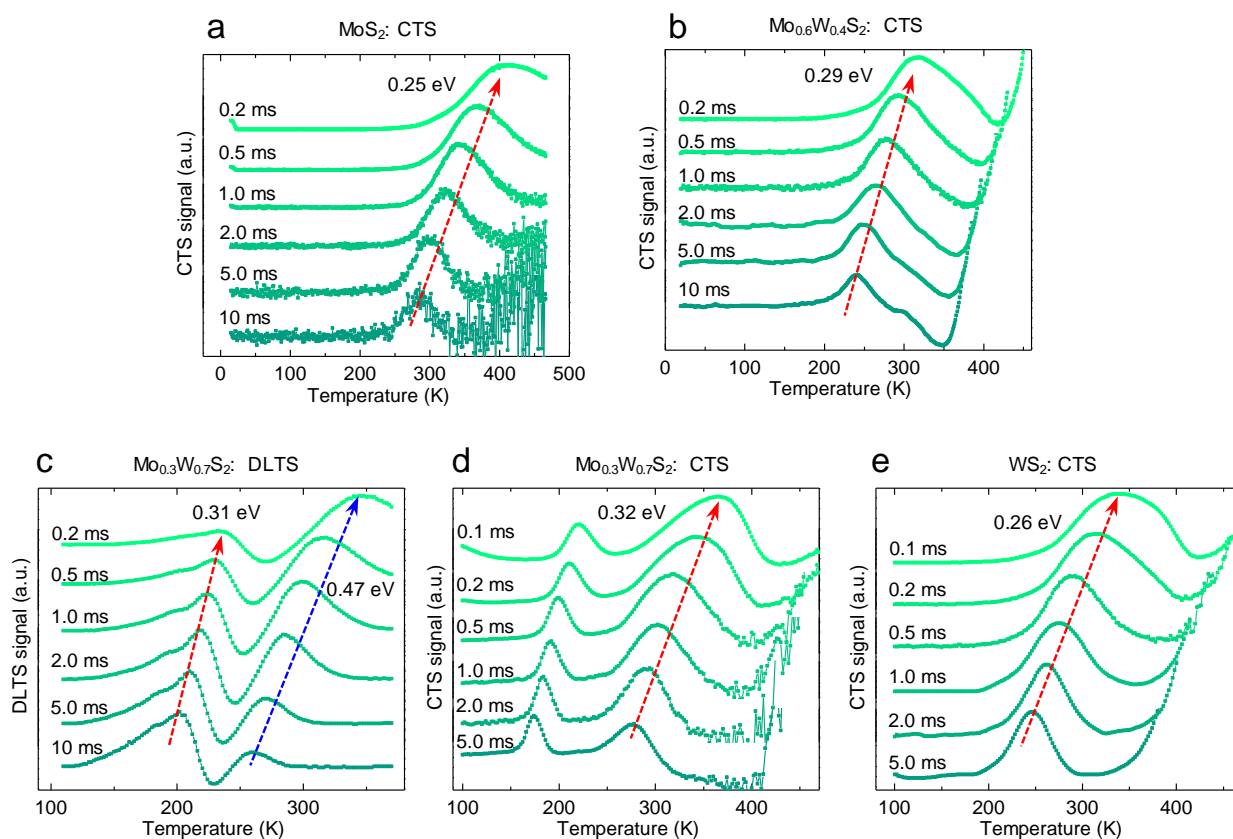


Open Access This article is licensed under a Creative Commons

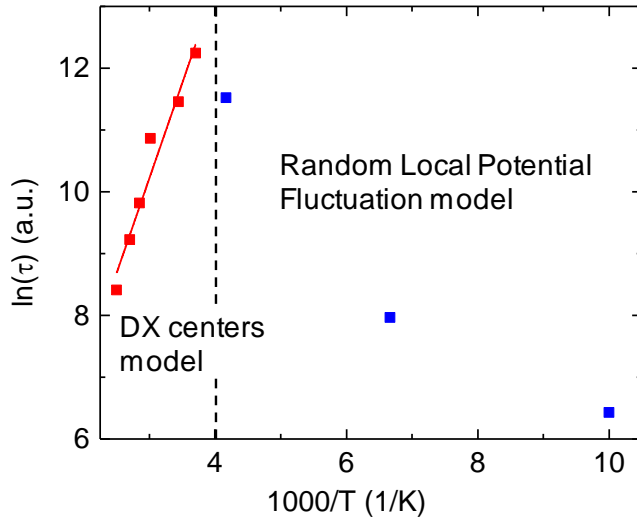
Attribution 4.0 International License, which permits use, sharing, adaptation, distribution and reproduction in any medium or format, as long as you give appropriate credit to the original author(s) and the source, provide a link to the Creative Commons license, and indicate if changes were made. The images or other third party material in this article are included in the article's Creative Commons license, unless indicated otherwise in a credit line to the material. If material is not included in the article's Creative Commons license and your intended use is not permitted by statutory regulation or exceeds the permitted use, you will need to obtain permission directly from the copyright holder. To view a copy of this license, visit <http://creativecommons.org/licenses/by/4.0/>.

© The Author(s) 2020

Supplementary Information

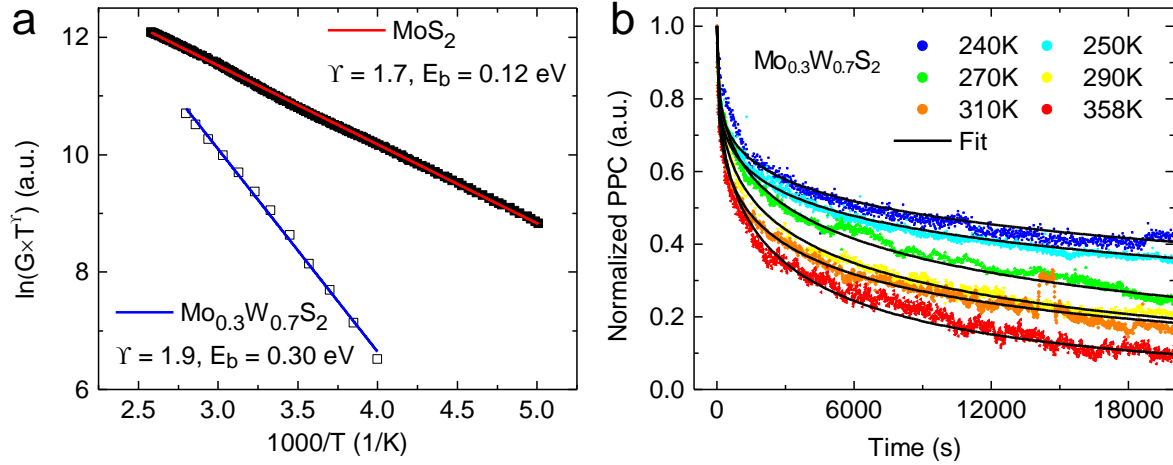


Supplementary Figure 1: DLTS and CTS data for Mo_{1-x}W_xS₂ crystals. The CTS spectra shows only the V_S feature but with asymmetrical profile, in particular for curves with the rate window below 1.0 ms. The asymmetric shoulder at higher temperatures in the CTS spectra suggests a deeper energy level too weak to be analyzed, and is possibly caused by the DX center. The CTS spectrum of Mo_{0.3}W_{0.7}S₂ in Supplementary Fig. 1d shows an additional feature at lower temperatures than that with the activation energy of 0.32 eV. Its origin is currently unknown.



Supplementary Figure 2: Arrhenius plot of PPC time constant for MoS₂ in the broad temperature range. The DX center model explains the expeditious decay of PPC in the high-temperature regime ($T > 270$ K). When $T < 240$ K, the time constant of MoS₂ instead drops with decrease in temperature, which is explained by random local potential fluctuation (RLPF), a model that was proposed in previous reports^{1,2}. In the RLPF model, random low-potential sites in the conduction band are spatially separated from those in the valence band, so photo-generated electrons (holes) tend to be trapped by these localized sites in the conduction (valence) band, which results in a long carrier lifetime and the PPC effect. These local potential fluctuation in the vdW materials could arise from disordered, charged native defects², or randomly distributed trapped charges on the SiO₂ substrate³. In details, at low temperatures (below ~ 100 K), photo-excited carriers are confined into these local sites and only contribute weakly to the current flow by hopping transport, hence leading to negligible PPC. As the temperature increases, more electrons gain sufficient kinetic energy to transfer from the localized states to delocalized states, forming a percolation network and thus contributing more to the conductivity, so the PPC effect becomes stronger and decays more slowly^{1,4}. Note that when the thermal energy is sufficiently high, it excites all localized electrons from the local potential sites, consequently the PPC effect tends to saturate, and its time constant becomes fixed or only weakly depend on temperature¹.

Indeed, the PPC effect can arise from more than one mechanism. For example, in ZnCdSe⁴, in the temperature range from 70 K to 220 K, the time constant of PPC rises with temperature because of the RLPF effect; but when $T > 220$ K, the time constant shows an opposite temperature dependence: the PPC decays faster as temperature grows. Both DX center and RLPF can cause the PPC effect but with distinct temperature dependencies. The energy barrier, E_c , of DX centers prevents photogenerated electrons from transferring to the localized DX centers, hence high temperature expedites the decay of the PPC. In contrast, in the RLPF mechanism, the local potential sites in the conduction band trap electrons that are frozen-out at low temperatures, thus, unlike DX centers, RLPF causes a faster decay of the PPC effect at lower temperatures.



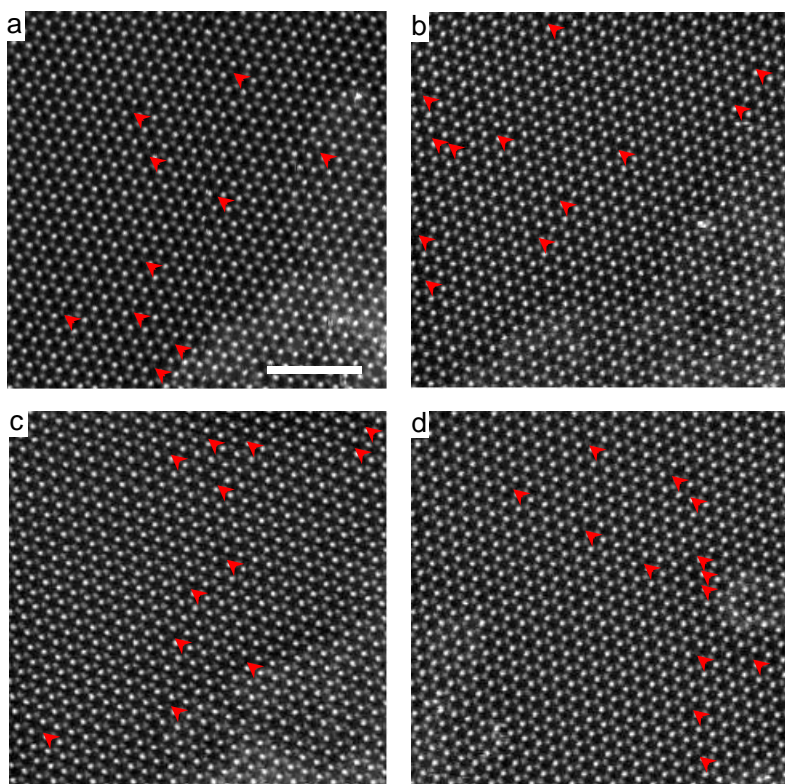
Supplementary Figure 3: Temperature-dependent conductivity and photoconductivity. a, Arrhenius plots of dark electron density ($n \propto G \times T^\gamma$) for MoS₂ and Mo_{0.3}W_{0.7}S₂ to determine binding energy E_b . **b,** Transient normalized-PPC curves at various temperatures for Mo_{0.3}W_{0.7}S₂, where the time constant is extracted by fitting with the stretched-exponential equation and shown in Fig. 3b.

We extract the thermal activation energy (E_b) for deep levels in MoS₂ and Mo_{0.3}W_{0.7}S₂ from the Arrhenius plot of the dark conductance versus inverse temperature as in Supplementary Fig. 3a. The carrier density (n) depends exponentially on temperature, $n \sim \exp(-E_b/k_B T)$, considering the Boltzmann distribution and the “full-slope” regime in the freeze-out curves of semiconductors, where only a small portion of the deep levels are ionized^{5,6}. On the other hand, conductivity can be expressed by the Drude model as $\sigma = n e \mu$, where μ is the mobility following a temperature dependence of $\mu \sim T^{-\gamma}$ above ~ 200 K as reported in previous studies⁷⁻⁹. Combining these equations, n is related to the conductance G and expressed as,

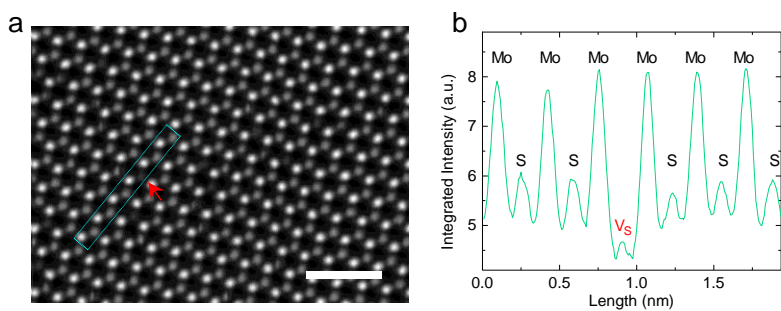
$$G \times T^\gamma \propto n \propto \exp\left(-\frac{E_b}{k_B T}\right). \quad (1)$$

Arrhenius plot of Supplementary Eq. (1) yields an activation energy of 0.12 eV for MoS₂ by using an exponent of $\gamma = 1.7$ as reported in literature⁸. We also found that the obtained value of E_b is insensitive to the value of γ used in the fitting, and only changes from 0.09 to 0.13 eV when γ is changed from 0.5 to 2.5. Similarly, we extract the activation energy of 0.30 eV for Mo_{0.3}W_{0.7}S₂ in Supplementary Fig. 3a, where γ uses the interpolated value of 1.9 following the known values of 1.7 for MoS₂ and 2.0 for WS₂^{8,9}.

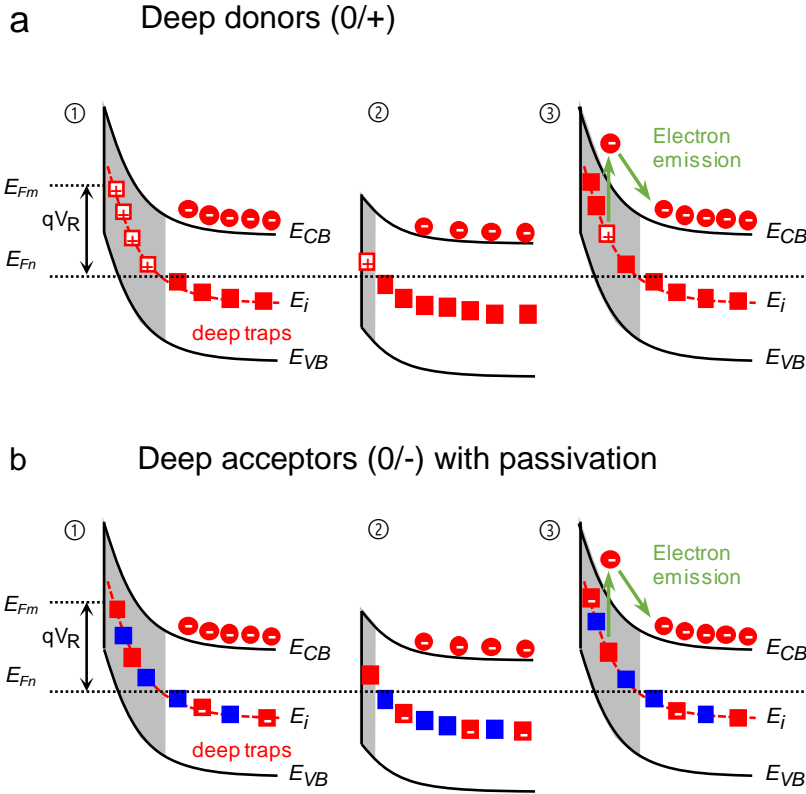
These E_b values (0.12 eV for MoS₂ and 0.3 eV for Mo_{0.3}W_{0.7}S₂) are shallower than the energy level E_i for sulfur vacancy (V_S) measured from E_{CB} . Therefore, they must originate from a defect level other than the V_S . As the only other deep level identified from DLTS is the DX centers, we assign the extracted E_b to the energy distance between E_{CB} and the E_{DX} . That is, $E_b = E_{CB} - E_{DX} = E_e - E_c$.



Supplementary Figure 4: Imaging V_S in monolayer MoS_2 with STEM. Scale bar, 2nm. V_S density is $\sim 0.2 \text{ nm}^{-2}$ in our exfoliated monolayer MoS_2 , corresponding to $\sim 3 \times 10^{20} \text{ cm}^{-3}$ in multilayers. Subtracting the S vacancies induced by the electron beam yields the native density of $> 1 \times 10^{20} \text{ cm}^{-3}$ (see methods in the main text), in agreement with literature^{10,11}.



Supplementary Figure 5: Intensity profiles of V_S in b, corresponding to the boxed region in a. Scale bar, 1 nm.



Supplementary Figure 6: Band bending of a n-type Schottky junction in response to the biased voltage for deep donors in a, and partly passivated deep acceptors in b. Blue blocks represent passivated (hence inactive and always neutral) deep acceptors. Stage ① - ③ correspond to those in Fig. 1c.

The concentration of V_S determined from STEM in Supplementary Fig. 4 is about $1 \times 10^{20} \text{ cm}^{-3}$ in MoS_2 , which is much higher than the free electron density of not intentionally doped MoS_2 on the order of $\sim 10^{18} \text{ cm}^{-3}$ as reported in literature^{7,12}. This could be attributed to either compensation or passivation of the deep levels, as widely observed and reported in many traditional semiconductors¹³⁻¹⁵. Supplementary Figure 6a presents the band bending of deep donors with full occupancy in the ground state, akin to the schematic in the main text. However, deep traps in semiconductors may be passivated, and hence de-activated at equilibrium, as shown in the case of deep acceptors in Supplementary Fig. 6b, leading to only a small portion of traps in the depletion zone being active and able to emit electrons under the reverse bias. The mechanism of passivation of the deep levels is currently unknown in MoS_2 , and is beyond the scope of this study, but the small capture cross section of V_S deep acceptors and their weak attraction to free electrons may play a role.

Supplementary Note 1: Calculation of deep level capture cross section from DLTS.

Rewriting Eq. (1) yields $\ln\left(\frac{T^2}{e_n}\right) = \ln\left(\frac{1}{K \cdot \sigma_n}\right) + \left(\frac{E_{CB} - E_i}{k}\right) \frac{1000}{T}$, where the extrapolation in the Arrhenius plot (Fig. 2b) allows extraction of the capture cross section, σ_n . The constant K is expressed as^{5,16}

$$K = 2 \left(\frac{2\pi m_e^* k}{h^2}\right)^{3/2} \left(\frac{3k}{m_{tc}^*}\right)^{1/2} = 3.26 \times 10^{21} \left[\frac{1}{\text{cm}^2 \text{K}^2 \text{s}}\right] \times \left(\frac{m_e^*}{m_{tc}^*}\right)^{1/2}, \quad (2)$$

where m_{tc}^* is the normalized thermal velocity effective mass, and m_e^* is the normalized density of states mass. The latter mass has been determined to be 0.50 (normalized to the free electron mass) as reported by previous studies¹⁷. The former mass is expressed as¹⁸

$$m_{tc}^* = \frac{4m_l}{[1 + \sqrt{m_l/m_t} \sin^{-1}(\delta)/\delta^2]^2}, \quad (3)$$

where $\delta = \sqrt{(m_l - m_t)/m_l}$, and m_l and m_t are the longitudinal and transverse effective masses in the ellipsoidal energy surface¹⁸. Our DFT calculation determines m_l and m_t to be 0.62 and 0.55, respectively, hence giving $m_{tc}^* = 0.57$. Finally, the capture cross section of V_S is calculated to be $\sim 3.6 \times 10^{-18} \text{ cm}^2$ in MoS_2 .

Supplementary Note 2: Impact of our results: prediction of deep levels of anion impurities.

The knowledge of V_S attained in this study can be used to understand and predict energy levels of anion-substitutional impurities such as oxygen in MoS₂ or WS₂. In order to explain this prediction, we start with discussing the bonding / antibonding model for a di-atomic system with the secular equation^{19,20}

$$\begin{vmatrix} E - E_{A0} & V \\ V & E - E_{B0} \end{vmatrix} = 0, \quad (4)$$

where E_{A0} and E_{B0} (lower than E_{A0}) are the atomic levels, and V is the interaction between E_{A0} and E_{B0} arising from the wavefunction overlap. Solving this equation yields two eigenvalues, corresponding to the molecular bonding and antibonding energy levels:

$$E_A = \frac{E_{A0} + E_{B0}}{2} + \frac{1}{2} \sqrt{(E_{A0} - E_{B0})^2 + 4V^2}, \quad (5)$$

and

$$E_B = \frac{E_{A0} + E_{B0}}{2} - \frac{1}{2} \sqrt{(E_{A0} - E_{B0})^2 + 4V^2}. \quad (6)$$

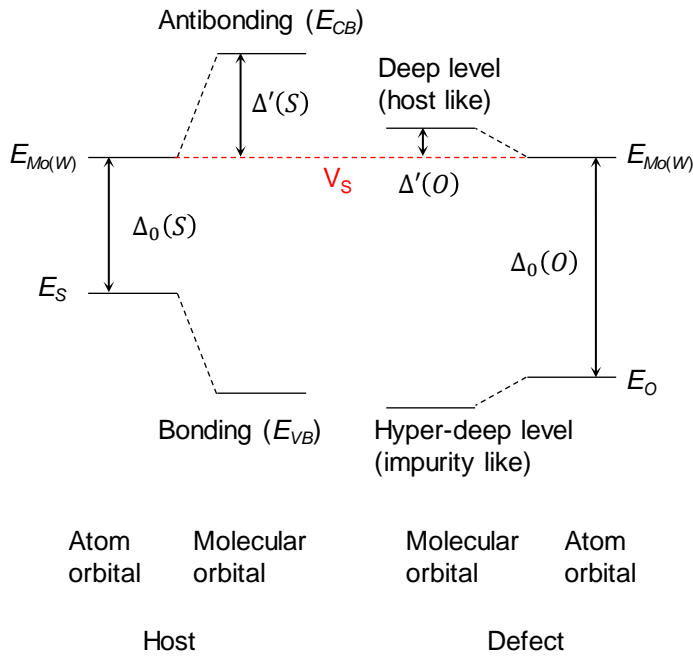
Then rewriting of Supplementary Eq. (4) gives

$$\Delta' = \frac{1}{2} \left(\sqrt{\Delta_0^2 + 4V^2} - \Delta_0 \right), \quad (7)$$

where $\Delta_0 = E_{A0} - E_{B0} > 0$ represents the energy difference between the initial atomic levels, and $\Delta' = E_A - E_{A0} > 0$ is the difference in energy between the atomic level and its originated molecular orbital (Supplementary Fig. 7). In order to determine the evolution of Supplementary Eq. (7) with the change in Δ_0 , the first-order differentiation is calculated as

$$\frac{d\Delta'}{d\Delta_0} = \frac{1}{2} \left(\frac{\Delta_0}{\sqrt{\Delta_0^2 + 4V^2}} - 1 \right) < 0, \quad (8)$$

indicating a monotonically decreasing function of Supplementary Eq. (7). This suggests that increase in the difference of the initial atomic levels will reduce the splitting between the atomic and molecular levels (Δ' , see Supplementary Fig. 7).



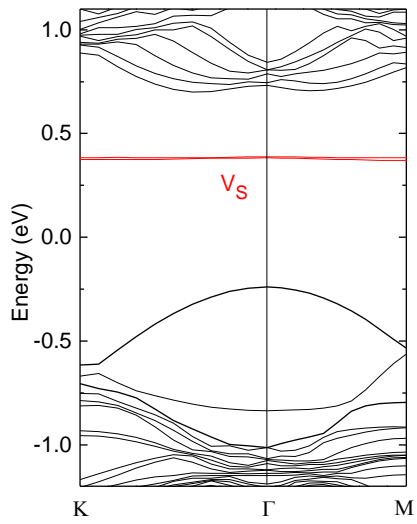
Supplementary Figure 7: Bonding / antibonding model explaining the formation of deep levels in the bandgap of MoWS₂. The left-hand side is schematic of the atomic levels of Mo(W) and S atoms and the resultant antibonding and bonding states in MoS₂ (WS₂). The right-hand side shows atomic level of the Mo(W) atom and substitutional O atom (defect) and the resultant deep and hyper-deep levels in MoS₂ (WS₂) with O defects.

Next, we discuss the formation of the energy level induced by more electronegative, anion substitutional impurities in MoS₂ or WS₂ in Supplementary Fig. 7. The left-hand side presents the creation of conduction and valence bands in MoS₂ following the simplest possible bonding / antibonding model. We note that, according to the origins of conduction band maximum (CBM) and the valence band minimum (VBM) in MoS₂ or WS₂²¹, the antibonding state (E_{CB}) in Supplementary Fig. 7 can be defined as the CBM, while the bonding state (E_{VB}) is deeper than the VBM, so the difference between E_{CB} and E_{VB} is not equal to the bandgap. The energy difference between the atomic level of Mo(W) atom and the formed conduction band of Mo(W)S₂, $\Delta'(S)$, can be expressed by Supplementary Eq. (7). As calculated by DFT in Fig. 2d, the wavefunction of V_S is composed mainly of orbitals of Mo(W) atoms, hence it is reasonable to assume that the position of V_S level lies very close to the atomic level of Mo(W), $E_{Mo(W)}$, in Supplementary Fig. 7. Considering anion impurities such as oxygen substituting S in MoWS₂, the interaction between the O atom and its neighboring Mo(W) atoms forms two molecular levels, a deep level and a so-called hyper-deep level²². The latter is below the valence band and electrically inactive; in contrast, the former lies inside the bandgap and its wavefunctions is dominated by that of Mo(W), so it is called host-like defect level as shown in the right-hand side of Supplementary Fig. 7, akin to the nitrogen defect in GaP^{22,23}.

The low-lying oxygen atomic level with respect to the vacuum level means a more significant difference in the original energies ($\Delta_0(O) = E_{Mo} - E_O$) than that in host materials ($\Delta_0(S) = E_{Mo} - E_S$), resulting in the smaller splitting $\Delta'(O)$ in Supplementary Fig. 7, following the Supplementary Eq. (7) and (8). Due to the high electronegativity of O atom, the Mo(W)-O can form a more ionic bond with weaker wavefunction overlap and hence a smaller value of V (Supplementary Eq. (7)),

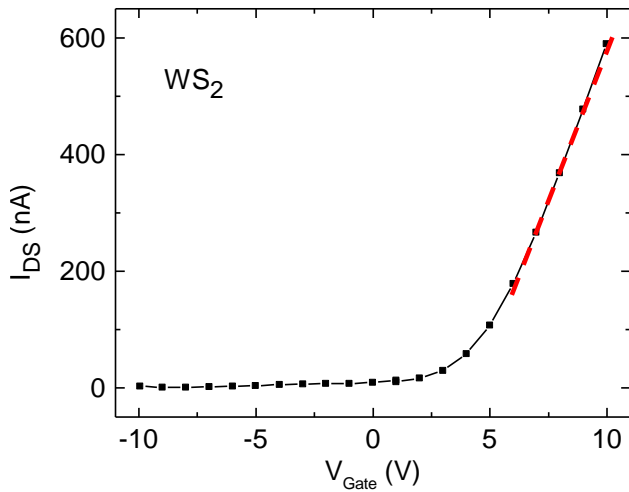
compared to the more covalent Mo(W)-S bond. In summary, it is reasonable to predict that anion impurities would create deep levels with similar energies as the V_S , about 0.3 eV below the CBM, in $Mo_{1-x}W_xS_2$ of all compositions.

Finally, the analysis above is not limited to Mo(W) disulfides; all other transition metal chalcogenides may be similarly discussed in the context of native defect energies once the anion vacancy level is measured.



Supplementary Figure 8: Band structure of multilayer MoS₂ with sulfur vacancies by DFT calculations, where V_S indicates the energy level of sulfur vacancies.

Supplementary Note 3: Characterization of vdW crystals Field-effect transistors.



Supplementary Figure 9: Source-drain current (I_{DS}) in response to the gate voltage (V_{Gate}) of field-effect transistors (FET) made of WS_2 at room temperature.

It is known that undoped MoS_2 has a native electron density over orders of magnitude higher than in WS_2 ^{24,25}. Here we explain it using the chemical trend of DX centers in these materials.

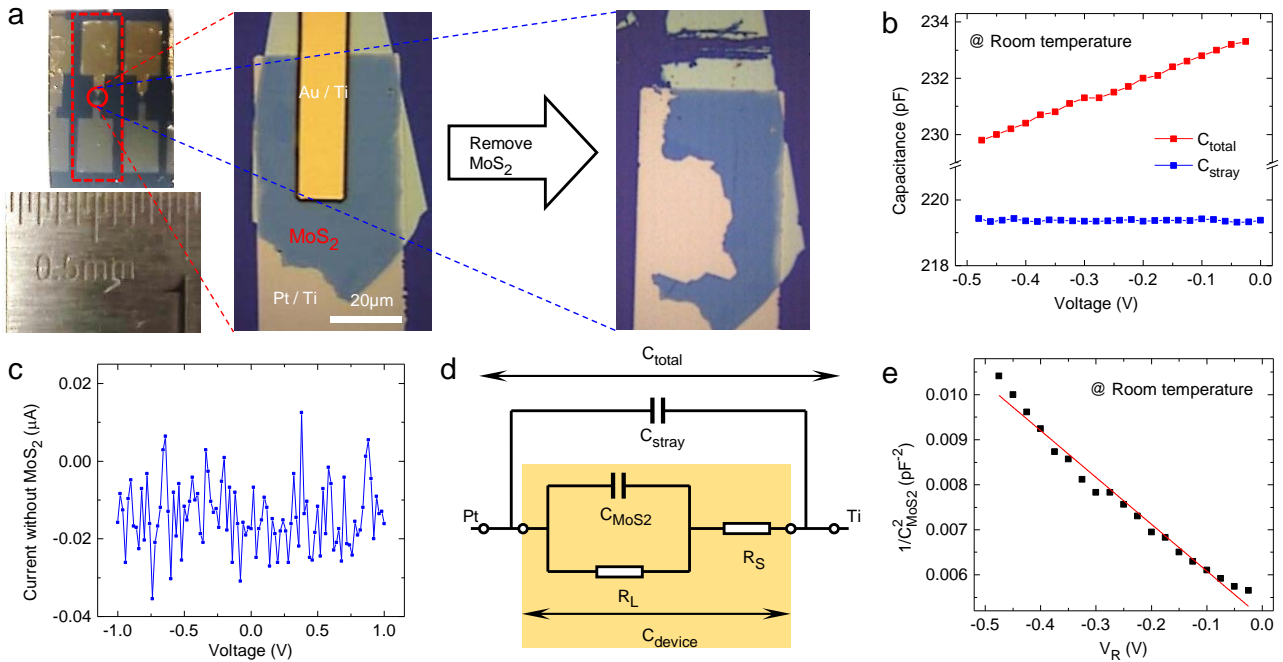
According to the data in Fig. 5b, we can extract the low-field field-effect mobility to be ~ 16 $cm^2/(V \cdot s)$ for MoS_2 . Thus, the free carrier density ($n = 1/(e \cdot \mu \cdot \rho)$) of MoS_2 is calculated to be $\sim 4 \times 10^{17} cm^{-3}$, consistent with results in previous studies^{12,24}. Similarly, the free electron concentration of WS_2 is determined to be $7 \times 10^{13} cm^{-3}$ by the FET results in Supplementary Fig. 9, also in good agreement with literature²⁵.

Next, we discuss the effect of DX centers on the free carrier density in MoS_2 and WS_2 . We assume the native donor density is on the same level in these two materials, but they are compensated to different extents by the DX centers as deep traps, because of their different energy depths in the bandgap of the hosts. Supplementary Equation 1 is then used to estimate the carrier density ratio of MoS_2 to WS_2

$$\frac{n(MoS_2)}{n(WS_2)} = \exp\left(\frac{E_b(WS_2) - E_b(MoS_2)}{k_B T}\right), \quad (9)$$

where $E_b(MoS_2) = 0.12$ eV is the energy depth of DX centers in MoS_2 , $E_b(WS_2)$ can be found by extrapolation to be ~ 0.38 eV based on the value of MoS_2 and $Mo_{0.3}W_{0.7}S_2$ in Fig.4c, and $k_B T = 26$ meV at room temperature. Therefore, we obtain free carrier density ratio ($n(MoS_2)/n(WS_2)$) to be $\sim 2 \times 10^4$ due to the charge compensation by DX centers. This is on the same order of magnitude as the value (5×10^3) determined from FET measurements.

Supplementary Note 4: Stray capacitance analysis and capacitance-voltage characterization.



Supplementary Figure 10: Stray capacitance analysis and capacitance-voltage

characterization. **a.** Optical image of an empty DLTS device for determination of parasitic capacitance by removing the flake of vdW material with a needle. The red circle represents the stacked parallel capacitor region with / without the flake of vdW material. **b.** Total capacitance (C_{total} , with flake) and stray capacitance (C_{stray} , removing flake) as a function of reverse bias at room temperature for the device in Supplementary Fig. 10a. **c.** Leakage current of the empty device in response to the bias voltage. **d.** Equivalent circuit of the device in Fig. 1a and Supplementary Fig. 10a. The yellow region represents the Schottky barrier circuit, showing a depletion capacitance of MoS₂ (C_{MoS2}) with a parallel leakage resistance (R_L) and series resistance of the non-depleted region (R_S). **e.** $1/C_{\text{MoS2}}^2$ vs. reverse voltage to characterize the dopant concentration for the device in Supplementary Fig. 10a at room temperature.

In order to fit the DLTS instrument, the electrodes of devices were designed to be on the size of several millimeters (Supplementary Fig. 10a), but the sample area is about tens of micrometers (Fig. 1a), so the large electrodes inevitably introduce parasitic coplanar capacitance, called stray capacitance, (Supplementary Fig. 10 b and d), whose magnitude is difficult to theoretically estimate due to the irregular geometry. This stray capacitance, even with a large value, is understandably insensitive to the external bias voltage, thereby not affecting the DLTS signal, because the DLTS records the differential capacitance within a rate window under reverse bias (Fig. 1c). Meanwhile, the weak, constant leakage current ($\sim 0.02 \mu\text{A}$, Supplementary Fig. 10c) in the empty device (Supplementary Fig. 10a) ensures the accuracy and reliability of the CTS measurements in Supplementary Fig. 1.

We can determine the MoS₂ capacitance by measuring the difference between total capacitance (C_{total} , with sample) and stray capacitance (C_{stray} , removing sample) in Supplementary Fig. 10 a and b, so the curve of $1/C_{\text{MoS2}}^2$ vs. V_R in Supplementary Fig. 10e allows us to obtain the built-in potential

(Φ_{bi}) of ~ 0.5 V for MoS₂/Pt Schottky diode and the dopant concentration of $\sim 3 \times 10^{18}$ cm⁻³ in nominally not intentionally doped MoS₂ (N_d) at room temperature, via its intercept and the slope according to²⁶

$$\frac{1}{C_{MoS_2}^2} = \frac{2(|\Phi_{bi}| + |V_R|)}{qN_d\epsilon_r\epsilon_0A^2}, \quad (10)$$

where $\epsilon_r = 11$ is the dielectric constant of multilayer MoS₂²⁷, V_R is the reverse biased voltage (Fig. 1c), A is the area of the depletion zone, and C_{MoS_2} is close to C_{device} ($= C_{total} - C_{stray}$). These two extracted parameters for MoS₂ are consistent with previous results in literature^{7,12,28}. As a result, the depletion width of the Schottky junction can be expressed as²⁶

$$W = \sqrt{\frac{2\epsilon_r\epsilon_0(|\Phi_{bi}| + |V_R|)}{qN_d}}, \quad (11)$$

and estimated to be ~ 22 nm under the reverse bias of 0.5 V at room temperature. Note that the dopant concentration determined here is significantly higher than the free electron density measured by FET in Supplementary Fig. 9, which is attributed to the trapping of free electrons by DX centers.

The linear $1/C^2$ vs. V_R curve indicates a roughly uniform distribution of dopants and nearly step junction profile of space charge density near the surface of the MoS₂/Pt Schottky diode^{16,29}, hence confirming the feasibility of Supplementary Eq. (11) to extract the depletion width.

Although it is reasonable to assume a nearly step junction profile for the space charge, in reality the free carrier density varies exponentially within the depletion zone, so a Debye screening length (or Debye tail, Debye incursion) is defined to express the abruptness of the space charge distribution near the edge of the depletion zone, which can be written as¹⁶

$$L_D = \sqrt{\frac{\epsilon_r\epsilon_0kT}{q^2N_d}}. \quad (12)$$

In our case, the high dopant concentration ($N_d \sim 3 \times 10^{18}$ cm⁻³) yields a Debye length of ~ 2 nm at room temperature, which is on the same order with that in heavily doped silicon¹⁶. The depletion width (~ 22 nm) is more than ten times greater than this Debye length, which in turn justifies the sharp, nearly step - function profile of space charge¹⁶.

In the above description, we assume that C_{MoS_2} is almost equal to C_{device} by omitting the effect of the leakage resistance (R_L) and the series resistance (R_S). When subtracting the parallel stray capacitance, the measured capacitance, C_{device} in the circuit within the yellow shadow (Supplementary Fig. 10d), is related to C_{MoS_2} by¹⁶

$$\frac{C_{MoS_2}}{C_{device}} = \left(1 + \frac{R_S}{R_L}\right)^2 + \left(\frac{R_S}{1/\omega C_{MoS_2}}\right)^2, \quad (13)$$

where ω is the frequency of a.c. voltage during the capacitance measurement and is 1 MHz in our case. Accurate test of the depletion capacitance and hence the depletion width requires that $R_S \ll R_L$ and $R_S \ll 1/\omega C_{MoS_2}$, such that the capacitive impedance, C_{MoS_2} , dominates the circuit element^{16,29,30}. The leakage resistance (R_L) and series resistance (R_S) can be approximately estimated from the reverse and forward bias current of the Schottky junction to be 80 k Ω and 2.5 k Ω under the reverse bias of 0.2V at 320 K (Fig. 1e), meeting the requirement of $R_S \ll R_L$. Given that $C_{MoS_2} \approx C_{total} - C_{stray}$, $1/\omega C_{MoS_2} = 77$ k $\Omega \gg R_S$ at 320 K. Therefore, Supplementary Equation (13) gives $C_{MoS_2} \sim C_{device}$, which justifies the reliability of the capacitance measurements. We note that the large leakage

current under reverse bias, called ‘soft’ reverse characteristics, may be attributed to the tunneling effect or the lowering of Schottky barrier height by image forces, as commonly reported in the Schottky junctions formed by low dimensional materials³¹⁻³³.

Supplementary Note 5: Thermodynamic interpretation of Arrhenius plots in DLTS.

The defect energy level in semiconductors is defined as the change of chemical potential due to the formation of a pair of charged carrier and ionized defect^{34,35}. The chemical potential thermodynamically means the variation of Gibbs free energy during the capture or emission of an electron at constant pressure and temperature. Thus, based on these definitions, the Arrhenius equation of the thermal emission rate in Eq. (1) can be rewritten as³⁵

$$\frac{e_n}{T^2} = K\sigma_n \exp\left(-\frac{\Delta G(T)}{k_B T}\right), \quad (14)$$

where $\Delta G(T) = |E_{CB} - E_i|$ and is the activation energy for electron emission from the deep state to the conduction band edge. At the same time, the Gibbs free energy is defined by the thermodynamic identity as $\Delta G(T) = \Delta H - T\Delta S$, where ΔH and ΔS represent the changes in enthalpy and entropy, respectively. Therefore, Supplementary Equation (14) becomes¹⁶

$$\frac{e_n}{T^2} = K\left[\exp\left(\frac{\Delta S}{k_B}\right)\sigma_n\right]\exp\left(-\frac{\Delta H}{k_B T}\right), \quad (15)$$

and hence the slope of the Arrhenius plot via Eq. (1) yields an average of enthalpy change over the temperature range of this plot, considering the generally weak temperature dependence of ΔH ¹⁶. The difference between ΔG and ΔH mainly arises from the lattice vibrational contribution to ΔS due to the coupling of occupied deep states to the lattice, and therefore, it is usually negligible when electrons are excited from the traps to conduction band without changing the bonding configuration ($\Delta S \sim 0$)³⁶. Thus, in this study, it is reasonable to consider the measured Arrhenius slope from DLTS as the activation energy for V_S states, because our DFT calculations do not observe lattice relaxation or entropy change during the transfer of electrons between the V_S defect and the conduction band edge.

With regard to DX centers, most of previous studies on group III-V semiconductors also neglected the difference between ΔG and ΔH ³⁷⁻⁴³, despite the occurrence of lattice relaxation when a DX center switches to the electron-donating state. In this study, we do not consider this difference for DX centers in vdW crystals. On the other hand, in order to obtain the exact activation energy, $\Delta G(T)$, via Supplementary Eq. (14), one needs to measure the values of both e_n and σ_n at desired temperatures. The emission rate, e_n , can be determined by the DLTS or transient capacitance test, while the capture cross section is usually measured using the diode short-circuiting technique^{44,45}, which is out of the scope of this study.

The main text and Supplementary Note 1 show the extraction of capture cross section, σ_n , of V_S deep state via the intercept of the Arrhenius plot in Fig. 2b. However, we note that, based on Supplementary Eq. (15), this intercept more accurately represents the product $\exp\left(\frac{\Delta S}{k_B}\right)\sigma_n$, rather than just σ_n . Experimentally, one could measure the latter using the diode shorting-circuiting technique^{44,45} to eventually determine the prefactor, ΔS , by temperature-dependent Gibbs free energy ($\Delta G = \Delta H - T\Delta S$).

Supplementary Note 6: Activation energy of DX centers by Arrhenius plot of DLTS.

Unlike regular deep levels which have no capture/emission barriers, such as the V_S state, for DX centers the Arrhenius plot of the DLTS spectrum extracts the emission barrier E_e , which is not the energy of the DX center directly measured from the conduction or valence band edges. This is because, in the case of DX centers, the energy barrier, E_c in the configurational coordinate diagram (CCD, Fig. 3c and 4c), must be overcome in order for an electron to be trapped by defects, hence leading to a strongly temperature-dependent capture cross section⁵,

$$\sigma_{n,DX} = \sigma_{\infty} \exp\left(-\frac{E_c}{k_B T}\right). \quad (16)$$

Combining Supplementary Eq. (16) and Eq. (1) gives

$$\frac{e_n}{T^2} = K\sigma_{\infty} \exp\left(-\frac{|E_{CB}-E_i|+E_c}{k_B T}\right), \quad (17)$$

where $|E_{CB} - E_i| + E_c$ is equal to the emission energy, E_e , in the CCD (Fig. 3c) without considering the entropy change, and E_i is E_{DX} .

To sum up, the DLTS spectrum measures the activation energy or binding energy (E_b) for normal defects such as the V_S states, while for DX centers, DLTS yields the emission energy (E_e), the summation of binding energy (E_b) and capture barrier (E_c).

Supplementary Note 7: Excluding a surface depletion mechanism for the PPC effect.

Although a surface depletion model was used to explain PPC effects in some low-dimensional systems^{46,47}, this model is unlikely to explain our observed PPC in MoS₂ and alloys. This is because PPC effects induced by surface depletion, for instance, in Si NWs or α -In₂Se₃ nanosheets^{46,47}, originate from self-assembled molecules on the surface or oxygen ions adsorbed from the environment. However, our STEM images (Fig. 1b) confirm the absence of adsorbents or contamination on the surface. Moreover, all the PPC tests were completed in high vacuum ($\sim 10^{-6}$ torr) after annealing at 400 K in vacuum for at least one day to remove possible adsorbents. In the meantime, such surface depletion mechanism usually induces only a weak PPC with a short decay constant (*e.g.*, \sim seconds at room temperature)⁴⁶, in stark contrast to the long PPC decay time we observed ($\sim 10^5$ s for multilayer MoS₂ at room temperature). Therefore, our PPC effect observed in MoS₂ and alloys is unlikely to be caused by any surface modification of the samples.

Supplementary References

- 1 Jiang, H. & Lin, J. Percolation transition of persistent photoconductivity in II-VI mixed crystals. *Physical review letters* **64**, 2547 (1990).
- 2 Wu, Y.-C. *et al.* Extrinsic origin of persistent photoconductivity in monolayer MoS₂ field effect transistors. *Scientific reports* **5**, 11472 (2015).
- 3 Xue, J. *et al.* Scanning tunnelling microscopy and spectroscopy of ultra-flat graphene on hexagonal boron nitride. *Nature materials* **10**, 282-285 (2011).
- 4 Jiang, H. & Lin, J. Persistent photoconductivity and related critical phenomena in Zn_{0.3}Cd_{0.7}Se. *Physical Review B* **40**, 10025 (1989).
- 5 McCluskey, M. D. & Haller, E. E. *Dopants and defects in semiconductors*. (CRC press, 2018).
- 6 Chand, N. *et al.* Comprehensive analysis of Si-doped Al_xGa_{1-x}As (x= 0 to 1): Theory and experiments. *Physical Review B* **30**, 4481 (1984).
- 7 Radisavljevic, B. & Kis, A. Mobility engineering and a metal-insulator transition in monolayer MoS₂. *Nature materials* **12**, 815-820 (2013).
- 8 Perera, M. M. *et al.* Improved carrier mobility in few-layer MoS₂ field-effect transistors with ionic-liquid gating. *ACS nano* **7**, 4449-4458 (2013).
- 9 Xu, S. *et al.* Universal low-temperature Ohmic contacts for quantum transport in transition metal dichalcogenides. *2D Materials* **3**, 021007 (2016).
- 10 Hong, J. *et al.* Exploring atomic defects in molybdenum disulphide monolayers. *Nature communications* **6**, 1-8 (2015).
- 11 Qiu, H. *et al.* Hopping transport through defect-induced localized states in molybdenum disulphide. *Nature communications* **4**, 1-6 (2013).
- 12 Radisavljevic, B., Radenovic, A., Brivio, J., Giacometti, V. & Kis, A. Single-layer MoS₂ transistors. *Nature nanotechnology* **6**, 147 (2011).
- 13 Lagowski, J., Kaminska, M., Parsey Jr, J., Gatos, H. & Lichtensteiger, M. Passivation of the dominant deep level (EL2) in GaAs by hydrogen. *Applied Physics Letters* **41**, 1078-1080 (1982).
- 14 Dautremont - Smith, W. *et al.* Passivation of deep level defects in molecular beam epitaxial GaAs by hydrogen plasma exposure. *Applied physics letters* **49**, 1098-1100 (1986).
- 15 Nability, J. *et al.* Passivation of Si donors and DX centers in AlGaAs by hydrogen plasma exposure. *Applied physics letters* **50**, 921-923 (1987).
- 16 Blood, P. & Orton, J. W. *The electrical characterization of semiconductors: majority carriers and electron states*. Vol. 2 (Academic press London, 1992).
- 17 Peelaers, H. & Van de Walle, C. G. Effects of strain on band structure and effective masses in MoS₂. *Physical Review B* **86**, 241401 (2012).
- 18 Green, M. A. Intrinsic concentration, effective densities of states, and effective mass in silicon. *Journal of Applied Physics* **67**, 2944-2954 (1990).
- 19 Ci, P. *et al.* Quantifying van der Waals interactions in layered transition metal dichalcogenides from pressure-enhanced valence band splitting. *Nano letters* **17**, 4982-4988 (2017).
- 20 Burns, G. *Solid State Physics*. (Elsevier Science, 1985).
- 21 Kang, J., Tongay, S., Zhou, J., Li, J. & Wu, J. Band offsets and heterostructures of two-dimensional semiconductors. *Applied Physics Letters* **102**, 012111 (2013).
- 22 Hjalmarson, H. P., Vogl, P., Wolford, D. J. & Dow, J. D. Theory of substitutional deep traps in covalent semiconductors. *Physical Review Letters* **44**, 810 (1980).
- 23 Yu, P. Y. & Cardona, M. *Fundamentals of semiconductors: physics and materials properties*. (Springer, 1996).
- 24 Kwak, J. Y. *et al.* Electrical characteristics of multilayer MoS₂ FET's with MoS₂/graphene heterojunction contacts. *Nano letters* **14**, 4511-4516 (2014).
- 25 Braga, D., Gutiérrez Lezama, I., Berger, H. & Morpurgo, A. F. Quantitative determination of the band gap of WS₂ with ambipolar ionic liquid-gated transistors. *Nano letters* **12**, 5218-5223 (2012).
- 26 Hu, C. *Modern semiconductor devices for integrated circuits*. Vol. 2 (Prentice Hall Upper Saddle River,

- New Jersey, 2010).
- 27 Chen, X. *et al.* Probing the electron states and metal-insulator transition mechanisms in molybdenum disulphide vertical heterostructures. *Nature communications* **6**, 6088 (2015).
- 28 Kim, G.-S. *et al.* Schottky barrier height engineering for electrical contacts of multilayered MoS₂ transistors with reduction of metal-induced gap states. *ACS nano* **12**, 6292-6300 (2018).
- 29 Pierret, R. F. *Semiconductor device fundamentals*. (Pearson Education India, 1996).
- 30 Goodman, A. M. Metal—Semiconductor barrier height measurement by the differential capacitance method—One carrier system. *Journal of Applied Physics* **34**, 329-338 (1963).
- 31 Kumar, S. *et al.* Influence of barrier inhomogeneities on transport properties of Pt/MoS₂ Schottky barrier junction. *Journal of Alloys and Compounds* **797**, 582-588 (2019).
- 32 Rhoderick, E. H. & Rhoderick, E. *Metal-semiconductor contacts*. (Clarendon Press Oxford, 1978).
- 33 Chen, C.-C., Aykol, M., Chang, C.-C., Levi, A. & Cronin, S. B. Graphene-silicon Schottky diodes. *Nano letters* **11**, 1863-1867 (2011).
- 34 Van Vechten, J. & Thurmond, C. Entropy of ionization and temperature variation of ionization levels of defects in semiconductors. *Physical Review B* **14**, 3539 (1976).
- 35 Thurmond, C. The standard thermodynamic functions for the formation of electrons and holes in Ge, Si, GaAs, and GaP. *Journal of the Electrochemical Society* **122**, 1133 (1975).
- 36 Almladh, C.-O. & Rees, G. Statistical mechanics of electronic energy levels in semiconductors. *Solid State Communications* **41**, 173-176 (1982).
- 37 Criado, J., Gomez, A., Munoz, E. & Calleja, E. Deep level transient spectroscopy signature analysis of DX centers in AlGaAs and GaAsP. *Applied physics letters* **49**, 1790-1792 (1986).
- 38 Calleja, E., Gomez, A., Munoz, E. & Camara, P. Fine structure of the alloy - broadened thermal emission spectra from DX centers in GaAlAs. *Applied physics letters* **52**, 1877-1879 (1988).
- 39 Kasu, M., Fujita, S. & Sasaki, A. Observation and characterization of deep donor centers (DX centers) in Si - doped AlAs. *Journal of applied physics* **66**, 3042-3046 (1989).
- 40 Calleja, E., Gomez, A. & Munoz, E. Direct evidence of the DX center link to the L - conduction - band minimum in GaAlAs. *Applied physics letters* **52**, 383-385 (1988).
- 41 Mooney, P., Theis, T. & Wright, S. Effect of local alloy disorder on emission kinetics of deep donors (DX centers) in Al_xGa_{1-x}As of low Al content. *Applied physics letters* **53**, 2546-2548 (1988).
- 42 Kumagai, O., Kawai, H., Mori, Y. & Kaneko, K. Chemical trends in the activation energies of DX centers. *Applied physics letters* **45**, 1322-1323 (1984).
- 43 Theis, T., Mooney, P. & Wright, S. Electron Localization by a Metastable Donor Level in n- GaAs: A New Mechanism Limiting the Free-Carrier Density. *Physical review letters* **60**, 361 (1988).
- 44 Brotherton, S. & Lowther, J. Electron and hole capture at Au and Pt centers in silicon. *Physical Review Letters* **44**, 606 (1980).
- 45 Brotherton, S. & Bicknell, J. The electron capture cross section and energy level of the gold acceptor center in silicon. *Journal of Applied Physics* **49**, 667-671 (1978).
- 46 Anandan, M. *et al.* High-responsivity broad-band sensing and photoconduction mechanism in direct-Gap α -In₂Se₃ nanosheet photodetectors. *Nanotechnology* **31**, 465201 (2020).
- 47 Zhao, X., Tu, P., He, J., Zhu, H. & Dan, Y. Cryogenically probing the surface trap states of single nanowires passivated with self-assembled molecular monolayers. *Nanoscale* **10**, 82-86 (2018).